AD-A039 245 TEXAS UNIV AT AUSTIN DEPT OF AEROSPACE ENGINEERING AN--ETC F/G 20/4
ANALYTICAL FLUTTER STUDIES OF A SUBSONIC, ACTIVELY CONTROLLED, --ETC(U)
MAR 77 L LEHMAN, R STEARMAN F44620-76-C-0072
UNCLASSIFIED AFOSR-TR-77-0637 NL

1 OF 2
AD A039245

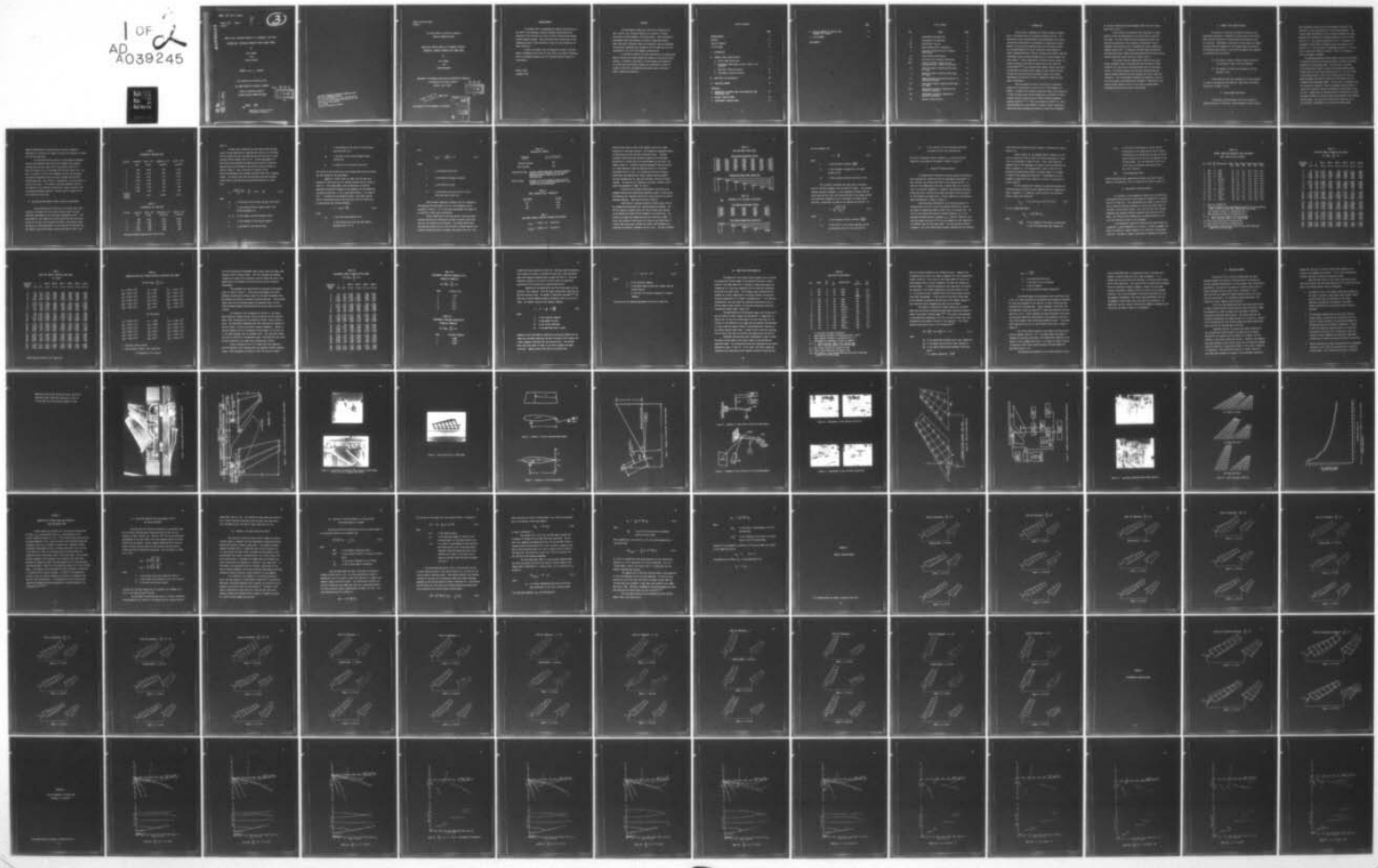

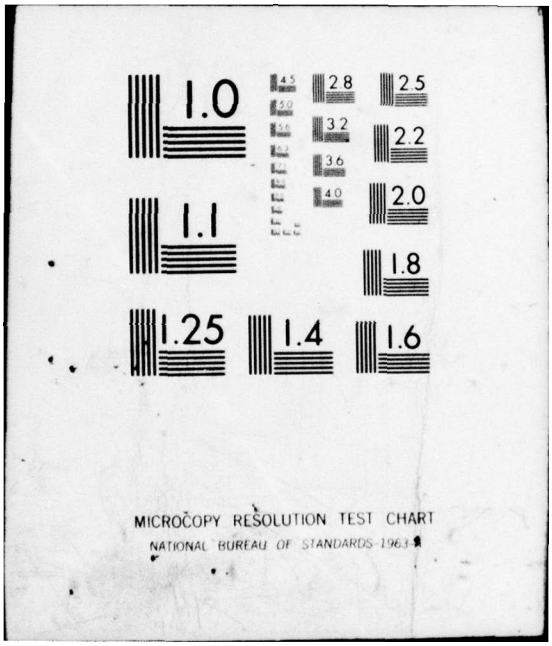
1.0
1.1
1.25
1.4
1.6
1.8
2.0
2.2
2.5
2.8
3.2
3.6
4.0
MICROCOPY RESOLUTION TEST CHART
NATIONAL BUREAU OF STANDARDS-1963-A

(3)

AFOSR FINAL Report
Volume I

ANALYTICAL FLUTTER STUDIES OF A SUBSONIC, ACTIVELY CONTROLLED, VARIABLE GEOMETRY WIND TUNNEL MODEL

by

Larry Lehman

and

Ronald Stearman

AFOSR FINAL REPORT

This research was sponsored by the

AIR FORCE OFFICE OF SCIENTIFIC RESEARCH

Office of Aerospace Research

through Contract F44620-76-C-0072

MARCH 1977

AIR FORCE OFFICE OF SCIENTIFIC RESEARCH (AFSC)
NOTICE OF TRANSMITTAL TO DDC
This technical report has been reviewed and is approved for public release IAW AFR 190-12 (7b).
Distribution is unlimited.
A. D. BLOSE
Technical Information Officer

AFOSR Scientific Report
Volume I

Air Force Office of Scientific Research

Contract F44620-76-C-0072

ANALYTICAL FLUTTER STUDIES OF A SUBSONIC, ACTIVELY CONTROLLED, VARIABLE GEOMETRY WIND TUNNEL MODEL

by

Larry Lehman

and

Ronald Stearman

Department of Aerospace Engineering and Engineering Mechanics

The University of Texas at Austin

Austin, Texas 78712

March 1977

sec 1473

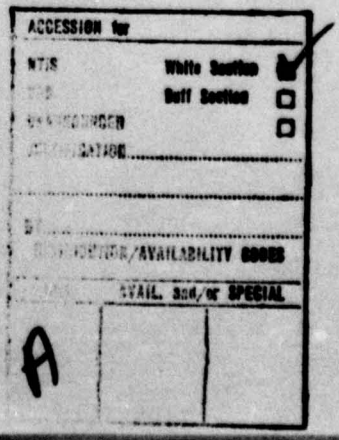

ACKNOWLEDGMENTS

The authors wish to acknowledge the support and assistance of the staff of the Aerospace Structural Dynamics and Aeroelasticity Laboratory of The University of Texas at Austin during the development of this research program. They also express their appreciation to the Computation Center of The University of Texas for the extended use of their facilities.

Finally, the authors wish to extend their thanks to William Walker, Aeromechanics Division, Air Force Office of Scientific Research, Office of Aerospace Research, for his continued financial supoort of this program.

Austin, Texas
September 1976

ABSTRACT

An experimental program was carried out to determine the mass, inertia, and stiffness properties of a subsonic, actively controlled, variable geometry, wind tunnel model. These experimental measurements were then employed to develop a lumped mass dynamic model from which vibrational modes and frequencies could be determined. The analytical modeshapes and frequencies of this model were verified experimentally for one of the geometry configurations.

An analytical analysis was then conducted for the uncontrolled model to predict the flutter speeds and frequencies during wind tunnel testing. In addition, the effect on flutter speeds and frequencies of various mass and stiffness changes was investigated in order to specify a final test configuration which would remain within the model's operating limitations.

TABLE OF CONTENTS

LIST OF TABLES

I. INTRODUCTION

Active control technology has recently become an integral part of the design process for advanced aerospace vehicles. The application of this new technology to high performance aircraft has necessitated investigation of new methods for analyzing and experimentally testing flutter suppression and load alleviation systems. The increased emphasis of control innovations being employed in Control Configured Vehicles (CCV) has indicated that dynamic stability requirements may be achieved through the use of active feedback control systems.[1] Flutter suppression of flexible lifting surfaces is a natural extension of the new CCV concept and initial analytical investigations[2,3,4] have indicated that feedback control laws could be developed to increase flutter speeds for both isolated lifting surfaces and aircraft wings with external stores. More recent experimental verification of flutter suppression systems has been shown in Reference 5.

With the support of the Air Force Office of Scientific Research and the assistance of the Air Force Flight Dynamics Lab (AFFDL), a graduate level research program was begun at The University of Texas to study active flutter suppression on interfering lifting surfaces using the latest and most accurate unsteady aerodynamic computer programs.[1,6,7,8] After the research of Griffin[7] on a small semirigid model with three degrees of freedom, flutter suppression control laws were developed and analyzed by Cwach[1] and Pinnamaneni[8]

for the more complicated variable-geometry AFFDL wing-tail flutter model shown in Fig. 1.

A wind tunnel test program was then undertaken to experimentally verify the effectiveness of an active control system for this model. The first stage of the test program consisted of the design and construction of the electronic and hydraulic control components which would be used to implement the flutter suppression feedback control laws.[6] In addition, the AFFDL model was modified and constructed with a remote wing sweep mechanism and a hydraulically actuated stabilator control surface as shown in Fig. 2.

The current study was undertaken to identify the system dynamic parameters and to investigate and tune the passive flutter properties for this actively controlled model prior to wind tunnel testing. The tuning procedures utilized mass redistribution and simple stiffness modifications which reduced the flutter speeds and frequencies. The system dynamic parameters are required as input to the active control law determination procedures.[1] Additionally, the passive flutter analysis results will be used to evaluate model performance during the wind tunnel testing phase.

II. DYNAMIC SYSTEM IDENTIFICATION

The objective in defining the dynamic system was to use experimental procedures to determine an accurate mass and stiffness model from which analytical vibration modes and frequencies could be calculated. Experimental verification of these modes and frequencies would then be attempted for the 60-degree sweep configuration. The following simplications in the analytical modeling were employed to facilitate this verification:

(1) The effects on model stiffness related to pressure in the hydraulic supply lines was neglected.

(2) The hydraulic cylinders were assumed to be rigid structural links.

These simplifications were accounted for in the experimental tests by disconnecting the hydraulic supply hoses and rigidly locking the cylinders in place.

A. Flutter Model Description

The actively controlled model used in this study is a modified version of a half-span, variable-geometry, passive flutter

model designed by the Air Force Flight Dynamics Laboratory[9] and consists of a wing, horizontal tail, and fuselage mechanism. The original model was modified to have a remotely operated wing sweep mechanism and a hydraulically actuated stabilator control surface (see Fig. 1). The supporting mechanism of Fig. 1 is encased in an aerodynamic housing which is mounted to the wind tunnel ceiling (see Fig. 3). Since the model is suspended on bearings, it is free to roll under the influence of gravity. That is, it possesses a rigid roll degree of freedom.

The fuselage mechanism and wing support structure was designed to allow easy variation of fuselage stiffness, wing-tail horizontal separations, and wing sweep angle. The wing spar is attached to the fuselage roll beam by a wing carry-through mechanism which contains both roll and pitch springs (see Fig. 2). The roll spring is positioned parallel to the roll axis while the pitch spring is swept 20 degrees from vertical (parallel to the elastic axis for 25-degree wing leading edge sweep). The tail spar is attached to the aft fuselage roll beam by a rigid carry-through structure which is fitted with a bearing to allow the stabilator to pitch about a vertical axis. Forward and aft fuselage sections are coupled by a torsion bar whose stiffness is varied by changing the spacing of the fuselage torsion clamps. The torsion bar interconnector (see Fig. 2) is not included in measurements of the effective spring length.

Geometry modifications include horizontal wing-tail separation (obtained by sliding the tail support along the aft fuselage roll beam) and variable wing sweep.

The wing construction consists of seven wooden aerodynamic sections with removable panels which are attached to the tapered aluminum spar near the center line of each section (see Fig. 4). Hence, the elastic axis is coincident with the spar center line. The spar is located at 37.5% of the streamwise chord for the 25-degree wing sweep configuration and at an angle 5 degrees less than the leading edge sweep. Each section is separated by a slot into which is placed a thin piece of foam rubber to provide aerodynamic sealing. The stabilator is of identical construction, except it contains only five wooden aerodynamic sections. The tail spar is located at the 37.5% stabilator chord line.

B. Experimental Measurement of Mass, Inertia, and Stiffness

Before assembling the wing and tail, the mass, mass static unbalance, and moment of inertia about the spar center line were determined experimentally for each wooden aerodynamic section. From measurements of spar dimensions at each section the mass and inertia values for the spar were calculated and added to the section values. The results of these measurements for the wing and tail sections and the flexible wing carry-through structure are shown in Table I and

TABLE I

EXPERIMENTAL WING MASS DATA

Section	Location* (ft)	Mass x 10^2 (slug)	Unbalance x 10^3 (slug-ft)	Inertia x 10^3 (slug-ft^2)
1	.229	2.390	.782	3.742
2	.625	2.194	.963	3.268
3	.969	1.881	.671	2.414
4	1.354	1.556	.604	1.767
5	1.719	1.299	.432	1.191
6	2.094	1.103	.257	.789
7	2.484	.992	.183	.541
Flexible Carry-Through	--	8.011	15.260	8.157

TABLE II

EXPERIMENTAL TAIL MASS DATA

Section	Location* (ft)	Mass x 10^2 (slug)	Unbalance x 10^3 (slug-ft)	Inertia x 10^3 (slug-ft^2)
1	.198	2.027	1.123	4.664
2	.552	1.632	1.019	2.451
3	.917	1.323	.735	1.480
4	1.271	.880	.394	.597
5	1.620	.524	.083	.216

*Distance measured along the spar from the root.

Table II.

The mass static unbalance for each section about the spar center line was determined by supporting the section on a knife-edge directly beneath the spar and measuring the force exerted at a known distance from the support (see Fig. 5). Inertia measurements for each section were performed by supporting the section as above and connecting the trailing edge to two springs of known stiffness as shown in Figure 6. Next, the period of vibration of the section was measured using a Bentley proximity sensor and a frequency counter. The inertia could then be calculated using the following formula which is derived from the equations of motion for a rigid body,

$$I_s = \frac{D^2(k_1 + k_2)}{\omega^2} - \frac{Wx}{\omega^2} - m_s D^2 - Mx^2 \qquad (2.1)$$

where

I_s is the section inertia about the spar (lb-in-sec^2)

D is the distance from the support point to the spring attachment (in)

k_1, k_2 are the support spring stiffnesses (lb/in)

ω is the frequency of oscillation (rad/sec)

W is the weight of the section (lbs)

x is the distance of the center of gravity above the pivot point (in)

m_s is the mass of the spring attachment device ($lb\text{-}sec^2/in$)

M is the mass of the section ($lb\text{-}sec^2/in$).

The inertia of the flexible wing carry-through about the pitch spring axis was measured in the same manner.

Moments of inertia about the model roll axis were also measured for the forward and aft fuselage sections and are listed in Table III. These measurements were accomplished by accurately measuring the pendulum frequency of the component and then measuring the angular deflection, θ, for a known applied force, F, as shown in Fig. 7. Provided that the deflection angle is kept small and the mirror is positioned close to the pivot axis, the roll inertia can be calculated by the following formulas,

$$\theta = \frac{1}{2} \tan^{-1} \left(\frac{d_B}{r}\right) \tag{2.2}$$

where

d_B is the laser beam deflection (in)

r is the distance over which the laser beam is deflected (ref. Fig. 7)

and

$$I_{roll} = \left(\frac{Fd}{\sin \theta} \right) / \omega^2 \qquad (2.3)$$

where

F is the applied force (lbs)

ω is the pendulum frequency (rad/sec)

θ is the deflection angle

d is the distance from the roll axis to the force application point (Ft)

With the model completely assembled, the roll frequencies were measured for wing sweeps of 25, 45, and 60 degrees and are presented in Table IV. All of the above measurements were made with the hydraulic supply hoses disconnected.

Elastic properties for the wing and tail spars were determined by measuring the bending and torsional influence coefficients with the root effectively cantilevered. The bending coefficients were measured directly with an LVDT that gave a voltage readout on an accurate integrating digital voltmeter (see Figures 8 and 10). The

TABLE III

FUSELAGE ROLL INERTIA

Component	$I_\theta \times 10$ (slug-ft^2)
*Forward Fuselage	.623
**Aft Fuselage	.275

*Forward Fuselage - Includes leading edge glove, wing carry-through structure and all components of the fuselage mechanism forward of the torsion spring interconnector.

**Aft Fuselage - Includes tail carry-through structure and all components of the fuselage mechanism aft of the torsion spring interconnector.

TABLE IV

MODEL PENDULUM (ROLL) FREQUENCIES

Wing Sweep	f_R (Hz)
25°	0.78
45°	0.84
60°	0.87

TABLE V

WING CARRY-THROUGH STRUCTURE INFLUENCE COEFFICIENTS

$C_{roll} = 5.8518 \times 10^{-4}$ (rad/in-lb)

$C_{pitch} = 4.9806 \times 10^{-4}$ (rad/in-lb)

deflection was taken at each of the spanwise stations for loads applied at all the other stations. The voltage was converted directly to deflections by using the LVDT calibration factor. Torsional influence coefficients were obtained by measuring the rotational deflection at a station due to an applied moment at that point (see Figures 9 and 11). An optical leverage technique[10] gave deflections of a laser beam which could be converted directly to rotational deflections with Eq. (2.2). All bending and torsional influence coefficients were measured for several applied loads and moments and then averaged over all loads and reciprocal deflection loading stations. The wing and tail bending and torsional influence coefficients are presented in Tables VI and VII.

Pitch and roll influence coefficients of the wing carry-through structure were determined by applying a moment to each spring and measuring the rotational deflection of the spring with an optical leverage technique. These data are given in Table V.

Definitions of fuselage torsional stiffness versus torsion bar length were obtained with the fuselage mechanism assembled. The aft roll beam was clamped rigidly and load increments were applied to the forward roll beam creating a moment on the torsion bar. The torsion bar length was changed by moving the torsion bar clamps. A mirror was attached to the forward roll beam and the deflections of a laser light source were recorded for several load increments and converted to rotational increments with Eq. (2.2). Torsional stiffness

TABLE VI

WING INFLUENCE COEFFICIENTS

Wing Bending Along Spar (in/lb)

.0004	.0011	.0018	.0025	.0032	.0039	.0047
.0011	.0056	.0100	.0149	.0197	.0244	.0295
.0018	.0100	.0214	.0340	.0466	.0591	.0722
.0025	.0149	.0340	.0615	.0883	.1158	.1443
.0032	.0197	.0466	.0883	.1385	.1884	.2409
.0039	.0244	.0591	.1158	.1884	.2748	.3649
.0047	.0295	.0722	.1443	.2409	.3649	.5176

Wing Torsion About Spar (rad/in-lb)

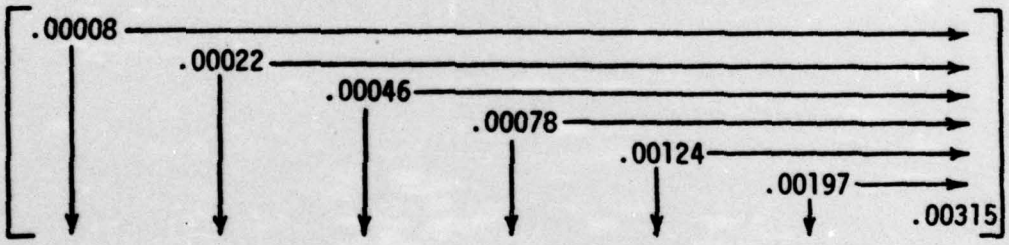

TABLE VII

HORIZONTAL TAIL INFLUENCE COEFFICIENTS

Tail Bending Along Spar (in/lb)

.0004	.0010	.0015	.0022	.0027
.0010	.0045	.0085	.0125	.0165
.0015	.0085	.0199	.0320	.0444
.0022	.0125	.0320	.0589	.0872
.0027	.0165	.0444	.0872	.1446

Tail Torsion About Spar (rad/in-lb)

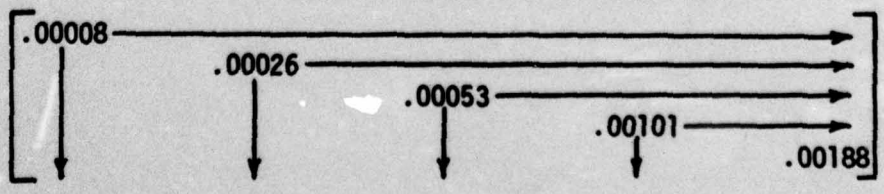

was then computed from

$$K = \frac{\Delta T}{\Delta \theta} \tag{2.4}$$

where

K is the torsional stiffness $(\frac{\text{in-lb}}{\text{rad}})$

ΔT is the increment of moment due to an added weight (in-lb)

$\Delta \theta$ is the resulting rotational deflection (rad).

This stiffness information was then used to calculate a curve of torsional frequency versus torsion bar length. The uncoupled fuselage torsional frequency, ω_θ, was computed by assuming that the entire wing and tail units were rigid and acted as two lumped inertias. The vibrational frequency of such a two degree of freedom system which has a rigid body roll mode can be computed from (see Ref. 11)

$$\omega = \sqrt{\frac{K(I_F + I_A)}{I_F\, I_A}} \tag{2.5}$$

where

K is the fuselage torsional stiffness $(\frac{\text{ft-lb}}{\text{rad}})$

I_F is the inertia of the forward fuselage section and wing about the roll axis ($\text{lbs-sec}^2\text{-ft}$)

I_A is the inertia of the aft fuselage section and tail about the roll axis (lbs-sec^2-ft).

The curve of fuselage torsional frequency, ω_θ, versus torsion bar length for a wing sweep of 60 degrees is shown in Figure 16.

C. Analytical Vibration Analysis

The dynamic model from which the natural modes and frequencies were calculated was constructed from the experimental measurements of mass, inertia, and stiffness described in the preceding section. It consists of 28 lumped mass points and a flexible wing, tail, and fuselage. As outlined in Appendix A, a computer code determines the appropriate mass point locations and assembles the model flexibility matrix for the required wing sweep angle. The mass modeling for the 60-degree sweep configuration is shown in Figure 12.

Each wing sweep configuration in the vibration analysis is characterized by its roll, pitch, and fuselage flexibilities, and by the amount of lumped mass added to nodes 6 and 7 on the main wing. The ratio of the coupled wing cantliever bending frequency, ω_h, to the uncoupled fuselage torsional frequency, ω_θ, is used as a measure of the coupling between wing and tail[9] and can be computed for each combination of stiffness, mass and wing sweep angle. The wing cantilever bending frequency is the first flexible mode frequency obtained with the fuselage

rigid, while the fuselage torsional frequency is determined as shown in Section II.B.

Typical results for the computed natural frequencies of the first six modes are listed in Table VIII and the modeshapes for cases 2 and 9 are tabulated in Tables IX and X. Also, three dimensional computer plots of the modeshapes for several of the configurations are shown in Appendix B. The configurations listed in Table VIII were determined by modifications made to the dynamic model in an attempt to reduce flutter speeds and frequencies. An explanation of these attempts to reduce the flutter speed will be given in the section on flutter analysis.

For all configurations examined, the generalized masses and stiffnesses were calculated from the computed modes and frequencies as shown in Appendix A. In addition, inertia terms for the stabilator control surface were defined by[1]

$$m_{\delta_{r_j}} = \iint h_r(x,y)\, h_{\delta_j}(x,y)\, \bar{m}(x,y)\, dx\, dy \qquad (2.6)$$

or, for a lumped mass model,

$$m_{\delta_{r_j}} = \{h_A\}^T_r [\bar{M}] \{h_\delta\}_j$$

where

$\{h_A\}^T_r$ is the transpose of the vector of deflections of the r^{th} absolute mode (Ref. Appendix A)

$\{h_\delta\}_j$ is the vector of deflections on the j^{th} control surface due to a unit deflection of the j^{th} control. The deflections are defined over the area of the j^{th} control surface and are zero on the remainder of the lifting surface. (For the stabilator control this is the vector of distances from the pitch axis for a unit rotation.)

$[\bar{M}]$ is the lumped mass matrix.

Typical generalized mass, generalized stiffness, and control inertia terms for configurations 2 and 9 of Table VIII are given in Table XI.

D. Experimental Vibration Analysis

An evaluation of the mathematical modeling was carried out by experimentally measuring the flexible modes and frequencies for configuration 2 of Table VIII. This configuration was chosen for verification since it would be analyzed thoroughly in initial wind tunnel tests of the model's active control system. Also, only the first four flexible modeshapes were measured although frequencies were verified for five modes. The fifth flexible modeshape was not measured because of the very small deflection values at this frequency.

The experimental apparatus for measuring the natural modes and frequencies is shown schematically in Figure 13. In this arrangmment the model is excited by a shaker attached to the rigid tail carry-through structure. The model is tuned to each natural frequency by displaying

TABLE VIII

NATURAL VIBRATION FREQUENCIES FROM EXPERIMENTAL

MASS, INERTIA AND STIFFNESS**

No.	Sweep	$\frac{\omega_h}{\omega_\theta}$	Modification	†Mode 1 (Hz)	Mode 2 (Hz)	Mode 3 (Hz)	Mode 4 (Hz)	Mode 5 (Hz)	Mode 6 (Hz)
1	60°	.8	None	.87	3.7	8.1	14.2	19.0	21.5
2	60°	.6	None	.87	4.0	8.8	14.3	19.2	23.2
3	60°	.4	None	.87	4.3	9.8	14.4	19.2	26.5
4	60°	*	M1,(a.)	.85	3.7	8.2	14.1	18.6	22.3
5	60°	*	M2,(a.)	.84	3.5	7.8	13.9	18.2	21.9
6	60°	*	R,(b.)	.87	3.8	8.6	14.1	18.4	22.9
7	60°	*	P,(c.)	.87	3.9	8.5	13.4	19.1	23.1
8	60°	.6	PM,(d.)	.84	3.2	7.0	12.9	17.8	21.0
9	45°	*	None	.84	4.1	9.7	13.9	19.2	23.3
10	45°	#	PM,(d.)	.80	3.4	7.7	12.3	18.0	21.2
11	25°	*	None	.78	4.1	10.4	13.8	19.1	23.4
12	25°	#	PM,(d.)	.73	3.5	8.5	11.8	18.3	21.3

** (see also, Appendix B)

† Pendulum frequencies were experimentally measured for the unmodified model and then corrected when lumped masses were added.

* Same fuselage stiffness as configuration No. 2

Same fuselage stiffness as configuration No. 8

(a.) 1. 10% of wing mass added at tip trailing edge
2. 20% of wing mass added at tip trailing edge

(b.) Roll spring flexibility increased by 50%

(c.) Pitch spring flexibility increased by 50%

(d.) 50% increase in pitch spring flexibility and 20% of wing mass added at tip trailing edge.

TABLE IX

ANALYTICAL MODES OF MODIFIED AFFDL MODEL

60° Sweep , $\frac{\omega_h}{\omega_\theta} = 0.6$

Structural Control Point	X (FT)	Y (FT)	Mode 1 .87 Hz	Mode 2 4.0 Hz	Mode 3 8.8 Hz	Mode 4 14.3 Hz	Mode 5 19.2 Hz	Mode 6 23.2 Hz
1	.41	-.19	-.073	.013	.022	.213	-.017	-.055
2	.74	.04	-.103	.046	.013	.317	.043	.007
3	1.00	.26	-.131	.084	-.012	.375	.090	.070
4	1.30	.50	-.162	.139	-.080	.387	.106	.109
5	1.58	.74	-.193	.201	-.176	.307	.062	.056
6	1.87	.98	-.225	.272	-.303	.140	-.062	-.118
7	2.17	1.23	-.257	.351	-.460	-.094	-.262	-.386
8	-.00	.40	-.150	-.010	.293	-.087	.007	-.086
9	.33	.62	-.177	.023	.294	-.046	.079	.024
10	.62	.80	-.201	.063	.267	-.041	.141	.150
11	.95	1.00	-.227	.118	.197	-.072	.175	.249
12	1.27	1.19	-.252	.182	.086	-.161	.144	.256
13	1.59	1.39	-.277	.255	-.060	-.317	.027	.136
14	1.92	1.59	-.304	.335	-.239	-.521	-.171	-.106
15	.01	-.14	-.079	-.016	.118	.017	-.052	-.101
16	-.46	.05	-.103	-.011	.170	.008	-.031	-.099
17	-.17	-.43	-.042	-.023	.041	.031	-.085	-.103
18	2.88	-.15	-.078	-.082	-.038	.002	-.082	.097
19	3.05	.18	-.120	-.130	-.074	-.008	-.044	.079
20	3.23	.49	-.162	-.182	-.123	-.029	.086	-.030
21	3.39	.82	-.204	-.237	-.183	-.059	.296	-.223
22	3.56	1.14	-.245	-.293	-.250	-.096	.569	-.488
23	2.21	.40	-.149	-.155	-.069	.008	-.195	.237
24	2.50	.62	-.177	-.189	-.098	-.002	-.154	.223
25	2.77	.87	-.211	-.232	-.143	-.023	-.026	.123
26	3.03	1.11	-.242	-.276	-.198	-.054	.197	-.086
27	3.28	1.36	-.274	-.323	-.262	-.091	.488	-.374
28	2.39	0.00	-.097	-.100	-.043	.006	-.133	.153

TABLE X

ANALYTICAL MODES OF MODIFIED AFFDL MODEL

45° Sweep†

Structural Control Point	X (FT)	Y (FT)	Mode 1 .84 Hz	Mode 2 4.1 Hz	Mode 3 9.7 Hz	Mode 4 13.9 Hz	Mode 5 19.2 Hz	Mode 6 23.3 Hz
1	.44	-.07	-.079	.005	.050	.235	-.016	-.079
2	.70	.23	-.114	.033	.061	.319	.050	.002
3	.90	.51	-.147	.068	.042	.363	.105	.102
4	1.13	.82	-.183	.117	-.030	.374	.129	.167
5	1.34	1.12	-.219	.173	-.145	.312	.084	.107
6	1.55	1.43	-.255	.238	-.306	.183	-.042	-.080
7	1.78	1.75	-.293	.309	-.507	.003	-.233	-.333
8	-.11	.39	-.133	.000	.271	-.117	.000	-.084
9	.16	.68	-.167	.028	.292	-.099	.070	.027
10	.39	.93	-.197	.063	.275	-.107	.128	.150
11	.66	1.21	-.230	.111	.204	-.137	.156	.238
12	.91	1.48	-.260	.168	.079	-.206	.117	.216
13	1.17	1.75	-.292	.233	-.096	-.321	-.002	.070
14	1.44	2.03	-.325	.305	-.314	-.467	-.188	-.166
15	.01	-.14	-.071	-.014	.111	.021	-.053	-.109
16	-.46	.05	-.093	-.007	.155	.017	-.032	-.105
17	-.17	-.43	-.038	-.024	.046	.028	-.084	-.113
18	2.88	-.15	-.070	-.089	-.028	.001	-.083	.100
19	3.05	.18	-.108	-.143	-.058	-.009	-.044	.083
20	3.23	.49	-.145	-.199	-.103	-.027	.087	-.026
21	3.39	.82	-.183	-.260	-.159	-.054	.299	-.226
22	3.56	1.14	-.221	-.322	-.221	-.087	.573	-.503
23	2.21	.40	-.134	-.169	-.049	.005	-.198	.241
24	2.50	.62	-.160	-.207	-.075	-.005	-.156	.231
25	2.77	.87	-.190	-.254	-.116	-.023	-.026	.132
26	3.03	1.11	-.218	-.303	-.168	-.050	.201	-.080
27	3.28	1.36	-.247	-.355	-.229	-.083	.494	-.380
28	2.39	0.00	-.088	-.110	-.030	.004	-.135	.156

† Same fuselage stiffness as 60° sweep case.

TABLE XI

GENERALIZED MASS AND STIFFNESS MATRICES OF MODIFIED AFFDL MODEL

60° Wing Sweep , $\frac{\omega_h}{\omega_\theta} = 0.6$

$m_{11} = 8.678 \times 10^{-3}$	$k_{11} = .2593$	$m^*_{\delta 1} = -3.105 \times 10^{-3}$
$m_{22} = 6.844 \times 10^{-3}$	$k_{22} = 4.421$	$m_{\delta 2} = -3.524 \times 10^{-3}$
$m_{33} = 9.536 \times 10^{-3}$	$k_{33} = 29.25$	$m_{\delta 3} = -2.477 \times 10^{-3}$
$m_{44} = 8.724 \times 10^{-3}$	$k_{44} = 70.13$	$m_{\delta 4} = -6.496 \times 10^{-4}$
$m_{55} = 7.558 \times 10^{-3}$	$k_{55} = 109.5$	$m_{\delta 5} = 2.405 \times 10^{-3}$
$m_{66} = 1.006 \times 10^{-2}$	$k_{66} = 212.8$	$m_{\delta 6} = -1.272 \times 10^{-3}$

45° Wing Sweep†

$m_{11} = 8.436 \times 10^{-3}$	$k_{11} = .2350$	$m^*_{\delta 1} = -2.796 \times 10^{-3}$
$m_{22} = 6.863 \times 10^{-3}$	$k_{22} = 4.586$	$m_{\delta 2} = -3.863 \times 10^{-3}$
$m_{33} = 9.278 \times 10^{-3}$	$k_{33} = 34.14$	$m_{\delta 3} = -2.089 \times 10^{-3}$
$m_{44} = 8.980 \times 10^{-3}$	$k_{44} = 68.10$	$m_{\delta 4} = -6.084 \times 10^{-4}$
$m_{55} = 7.545 \times 10^{-3}$	$k_{55} = 109.5$	$m_{\delta 5} = 2.436 \times 10^{-3}$
$m_{66} = 1.068 \times 10^{-2}$	$k_{66} = 229.7$	$m_{\delta 6} = -1.252 \times 10^{-3}$

* Stabilator control surface

† Same fuselage stiffness as 60° sweep case

All Dimensions in Ft. and Lbs.

on an oscilloscope the displacement sensor output versus the shaker load voltage to form a lissajou figure. With this procedure the resonant frequency for a mode can be accurately tuned by finding the point of 90 degree phase shift between the forcing function and the structural displacement.

The modeshapes were measured with an adjustable displacement sensor as shown in Figure 14. While these displacements were being measured, an additional proximity sensor at the shaker attachment point was monitored to maintain a constant excitation amplitude. This proximity sensor could also be displayed against the moveable sensor to check relative phasing between the excitation point and any other structural location.

As discussed in the introduction to Section II, the experimental modes and frequencies were initially measured with the hydraulic supply lines disconnected and the actuating cylinders locked rigidly in place. The experimental modeshapes were then normalized (see Appendix A) and are listed in Table XII with their resonant frequencies. Appendix C displays computer plots of the measured flexible modes, all of which are in very good agreement with the computed values. The calculated frequencies are all within 5% of the measured values, indicating that the elastic and mass properties of the model were simulated quite closely.

Natural frequencies for all six modes were then remeasured with the hydraulic lines connected while the actuator cylinders remained locked. These frequencies are given in Table XIII and are slightly

TABLE XII

EXPERIMENTAL MODES OF MODIFIED AFFDL MODEL

60° Sweep , $\frac{\omega_h}{\omega_\theta} = 0.6$

Structural Control Point	X (FT)	Y (FT)	Mode 2 4.2 Hz	Mode 3 9.0 Hz	Mode 4 15.1 Hz	Mode 5 19.2 Hz
1	.41	-.19	-.015	.014	.122	-.006
2	.74	.04	-.044	.010	.188	.041
3	1.00	.26	-.071	-.005	.233	.031
4	1.30	.50	-.129	-.046	.229	.031
5	1.58	.74	-.197	-.120	.146	.044
6	1.87	.98	-.293	-.235	.062	-.085
7	2.17	1.23	-.382	-.360	-.201	-.150
8	-.00	.40	.025	.257	-.083	.006
9	.33	.62	-.014	.269	-.087	.088
10	.62	.80	-.048	.235	-.097	.110
11	.95	1.00	-.111	.187	-.097	.132
12	1.27	1.19	-.172	.091	-.059	.119
13	1.59	1.39	-.229	.019	-.135	.081
14	1.92	1.59	-.322	-.178	-.302	-.038
15	.01	-.14	.018	.074	.021	-.056
16	-.46	.05	.036	.149	-.049	-.056
17	-.17	-.43	.025	.043	.028	-.078
18	2.88	-.15	.125	-.072	.056	-.213
19	3.05	.18	.122	-.096	-.010	-.138
20	3.23	.49	.172	-.168	-.104	-.025
21	3.39	.82	.236	-.252	-.264	.229
22	3.56	1.14	.315	-.351	-.469	.548
23	2.21	.40	.136	-.077	.111	-.279
24	2.50	.62	.189	-.130	.042	-.207
25	2.77	.87	.229	-.202	-.094	-.038
26	3.03	1.11	.279	-.274	-.274	.229
27	3.28	1.36	.307	-.360	-.472	.508
28	2.39	0.00	.096	-.050	.059	-.207

TABLE XIII

EXPERIMENTAL VIBRATION FREQUENCIES WITH

HYDRAULICS CONNECTED

60° Sweep , $\frac{\omega_h}{\omega_\theta} = 0.6$

Mode	Frequency (Hz)
1	1.45
2	4.2
3	9.1
4	15.8
5	19.0
6	22.0

TABLE XIV

EXPERIMENTAL STRUCTURAL DAMPING WITH

HYDRAULICS CONNECTED

60° Sweep , $\frac{\omega_h}{\omega_\theta} = 0.6$

Mode	Structural Damping
1	0.058
2	0.013
3	0.041

shifted from those appearing in Table XII, indicating that the hydraulic lines caused an increase in stiffness for the first, third and fourth modes while adding an apparent mass to modes five and six. These new modeshapes appeared to be similar to the old ones, but additional measurements will be necessary to quantify them exactly.

Damping was also measured for the first three modes with the hydraulic lines connected. With the shaker disconnected, modes one and two were excited by hand. The method of logarithmic decrement[12,13] was then used to obtain damping estimates from decay traces on an oscilloscope. For harmonic motion at the resonant frequency

$$g = 2\gamma = \frac{1}{N\pi} \cdot \ln\left(\frac{XP}{XQ}\right) \tag{2.8}$$

where

g is the structural damping

N is the number of cycles

XP is the initial amplitude

XQ is the amplitude after n cycles.

Damping for the third mode was obtained by exciting the model with the shaker and accurately measuring the phase lag angle of the response for slight frequency variations near the resonant point. The variable phase oscillator shown in Figure 13 was used to measure the phase variations. Damping values could then be calculated from

$$g = \tan \phi \, (1 - r^2) \qquad (2.9)$$

where

g is the structural damping

ϕ is the phase angle by which the response lags the forcing function

r is the ratio of excitation frequency to resonant frequency.

The results of the damping measurements are given in Table XIV.

III. ANALYTICAL FLUTTER ANALYSIS

The objective of the current flutter analyses was to evaluate the uncontrolled flutter speeds of the modified University of Texas version of the AFFDL model and, if necessary, reduce these speeds and frequencies to a level more compatible with the operating limitations during the wind tunnel tests. The 60 degree sweep configuration was examined for various combinations of fuselage stiffness and wing-tail horizontal separation, $\bar{X}$, as shown in configurations 1 - 6 of Table XV. Configuration 3 was then chosen for additional modification since it had the lowest flutter speed of all the cases possessing strong wing interference effects (small values of $\bar{X}$).

The modifications for the 60 degree sweep case included pitch and roll spring stiffness changes and the addition of lumped mass to nodes 6 and 7 at the tip trailing edge of the main wing (see Fig. 12). Criteria for the addition of the lumped mass was obtained from Reference 12, which shows the general effects of concentrated mass locations on the flutter speed of swept wings. As much as 20% of the total wing mass (10% in each of the outer two sections) was added during the analysis.

Additional configurations were investigated in order to study the effect of wing sweep on the flutter speeds of the modified and unmodified model. The configurations that were evaluated and the results obtained are given in Table XV. In all cases, the flutter speeds and frequencies were determined by the k-method of analysis using the zero

TABLE XV

ANALYTICAL FLUTTER RESULTS

No.	Sweep	$\frac{\omega_h}{\omega_\theta}$	$\bar{X}$ (ft)	Modification	V_F (ft/sec)	f_F (Hz)
1	60°	.8	.25	None	137	6.8
2	60°	.8	.90	None	140	6.4
3	60°	.6	.25	None	136 (162)†	7.3 (7.5)
4	60°	.6	.90	None	136	6.9
5	60°	.4	.25	None	140	8.0
6	60°	.4	.90	None	142	7.4
7	60°	*	.25	M1,(a.)	124	6.6
8	60°	*	.25	M2,(a.)	121	6.2
9	60°	*	.25	R,(b.)	139	7.0
10	60°	*	.25	P,(c.)	119	7.0
11	60°	.6	.25	PM,(d.)	107	5.7
12	45°	*	.99	None	155	7.2
13	45°	#	.99	PM,(d.)	107	4.9
14	25°	*	1.65	None	186	8.3
15	25°	#	1.65	PM,(d.)	150	4.9

$\bar{X}$ = Wing-Tail Horizontal Separation

* Same fuselage stiffness as configurations No. 3 and 4

\# Same fuselage stiffness as configuration No. 11

† Antisymmetric aerodynamics instead of symmetric

(a.) 1. 10% of wing mass added at tip trailing edge
2. 20% of wing mass added at tip trailing edge

(b.) Roll spring flexibility increased by 50%

(c.) Pitch spring flexibility increased by 50%

(d.) 50% increase in pitch spring flexibility and 20% of wing mass added at tip trailing edge

value of structural damping as the instability point. Computer plots of damping versus velocity are shown in Appendix D for the configurations listed in Table XV. Also, plots of the flutter modes for the 25, 45, and 60 degree cases are given in Appendix E for both the standard and modified models. It should be pointed out that these plots can display the character of the flutter eigenvector at only one instant of time ($t = 0$) and may not give a complete view of the flutter motion and possible node line movement. A true picture of the entire flutter mode can be obtained by displaying the real part of the complex response of each structural point throughout one entire cycle of motion.

The subsonic, uncontrolled, flutter analyses for the AFFDL model were carried out by formulating the flutter eigenvalue problem in terms of the natural vibration modes.[12,14] The current study employed, as the generalized coordinates, the first six natural modes, which were determined by the methods of Section II and Appendix A. The flutter equation could then be cast in the following form[19]

$$[K]^{-1} \left[[m] + g(\rho)\,[Q]\right] \{q\} = \lambda \{q\} \qquad (3.1)$$

where

$[K]$ is the generalized stiffness matrix (Ref. Appendix A)

$[m]$ is the generalized mass matrix (Ref. Appendix A)

$[Q]$ is the complex generalized aerodynamic coefficient matrix

λ is a complex eigenvalue, $\frac{1 + ig}{\omega^2}$

$g(\rho)$ is $\frac{C_r^2 S\rho}{2}$

C_r is the effective root chord

S is the area of the wing semispan

ρ is the air density

$\{q\}$ are the normalized complex eigenvectors

The unsteady generalized aerodynamic force coefficients used in Eq. (3.1) were calculated by the doublet-lattice method of Reference 20, which was developed for the analysis of planar interfering wing/horizontal-tail configurations. These aerodynamic coefficients were then modified as shown by Frederick[21] to make them compatible with the form of Eq. (3.1). Before computing the above aerodynamic force terms, the structural modes were interpolated to the aerodynamic grid with a local least squares fitting technique developed by Cwach.[1] The aerodynamic modeling for the 25, 45, and 60 degree sweep cases is shown in Figure 15.

All of the flutter analyses in the present study were evaluated for subsonic flow at M = 0.4. This Mach number was chosen to encompass all possible wind tunnel test regimes while remaining in the region of fully incompressible flow. It is shown for similar analyses in Reference 9 that flutter speed variations with Mach number are negligible below M = 0.5.

An additional consideration in the flutter analysis is that

the half-span AFFDL model is suspended such that it simulates anti-symmetric vibration modes and mirror image aerodynamics. It is assumed that the wind tunnel wall represents a reflecting plane through which no flow penetrates. This requires that the generalized aerodynamic forces be calculated assuming a symmetric loading since the image system is performing a symmetric motion to satisfy the flow boundary condition. Due to the antisymmetric vibrational characteristics and the symmetric aerodynamics, the current study approximates only the antisymmetric flutter modes under wind tunnel test conditions. For comparison, one test case was tried with antisymmetric aerodynamics and the results are given in Table XV and Appendix D.

IV. CONCLUDING REMARKS

The results of this study have demonstrated very good agreement between the analytical vibrational modes and frequencies and those obtained experimentally for the 60 degree sweep configuration. Additionally, the trends of the analytical vibration studies were in general agreement with the results given in References 1 and 9, indicating that the lumped mass dynamic modeling used in this study was quite satisfactory. All differences between experimental and theoretical results remained within 5 percent.

It has also been demonstrated that easily made modifications to model stiffness and mass could be used to reduce the flutter speeds and frequencies in order to remain within the model's operating limitations during wind tunnel testing. The flutter speed for the 60 degree configuration was reduced as much as 21 percent by a combination of decreasing the pitch spring stiffness and adding concentrated masses near the tip trailing edge of the wing.

Additional analysis for several wing sweep configurations has indicated that flutter speeds of the model can be increased substantially by sweeping the wing forward to 25 degrees, and thus removing it from close proximity to the tail. Therefore, the emergency wing sweep mechanism, which rapidly sweeps the wing forward on command, should be effective in stopping the flutter if any violent instability is encountered. The significant variations of flutter speed with wing sweep were attributed to changes in the aerodynamic interaction

between the wing and tail since all other model parameters were constant as the geometry was altered. In all of the configurations analyzed, the mode of instability remained the same.

When using the results of this study to determine control laws and to predict the wind tunnel behavior of the actively controlled model, the following things should be considered:

1. The hydraulic links in the dynamic model were considered to be rigid; in actuality, they possess some stiffness characteristics which were not determined in this study. Additional experimental investigation of the model's dynamic properties with a pressurized control system is desirable.

2. The aerodynamic modeling used in the flutter analyses assumes smooth, uniform flow over the wing and tail and does not include the effects of interference between the fuselage housing and the wing-tail combination. Studies of the flow properties around the model for a particular wind tunnel installation will be required to assess the validity of these assumptions and additional aerodynamic fairings may be required to produce desirable flow qualities.

3. Previous experience has shown the doublet-lattice aerodynamic code used in this study to be conservative in predicting flutter speeds. Also, since the zero value of structural

damping was used as the instability point, some of the indicated flutter speeds may increase by as much as 5 ft/sec when the true structural damping is used.

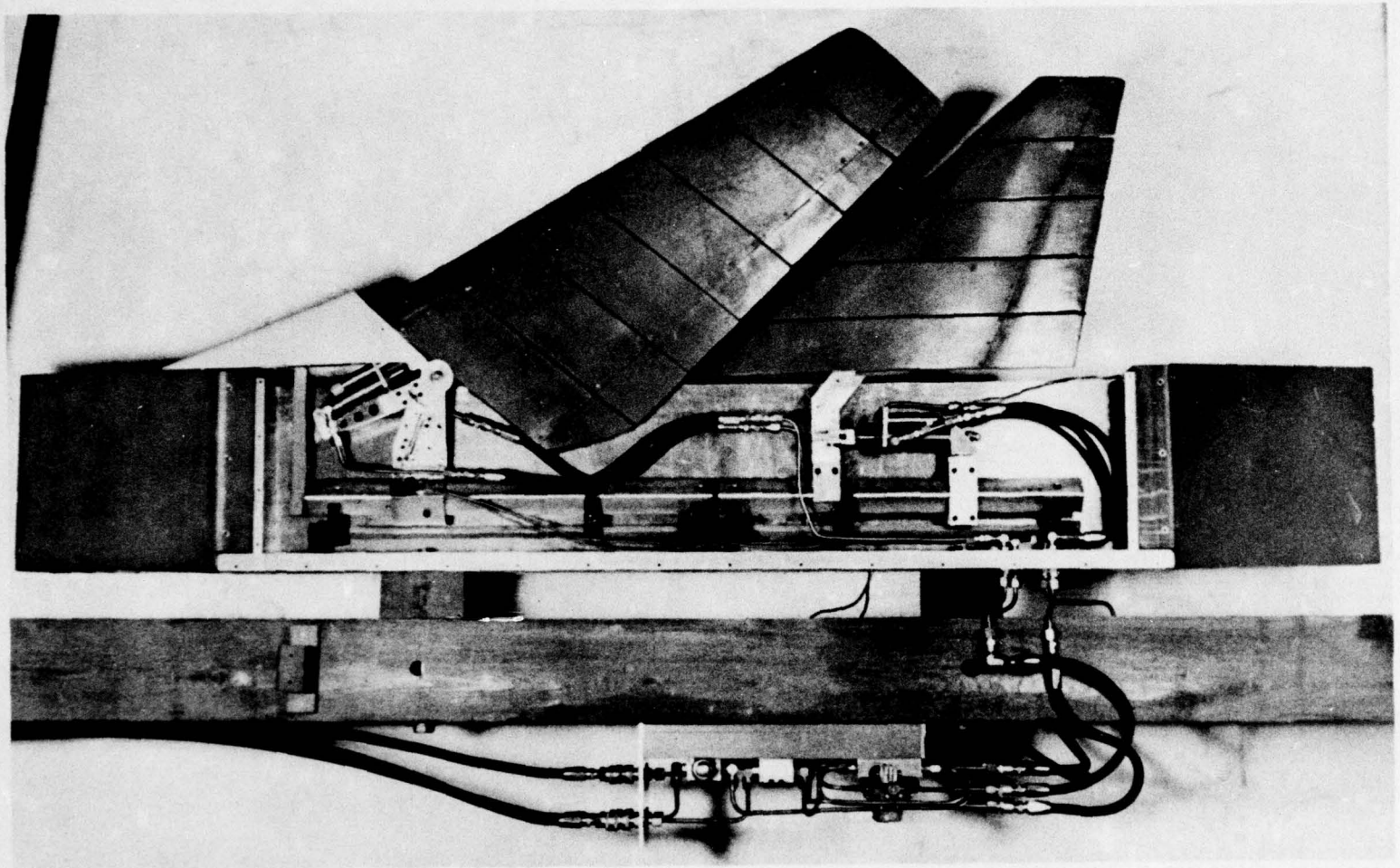

Figure 1. AFFDL Model Modified for Active Stabilator Control

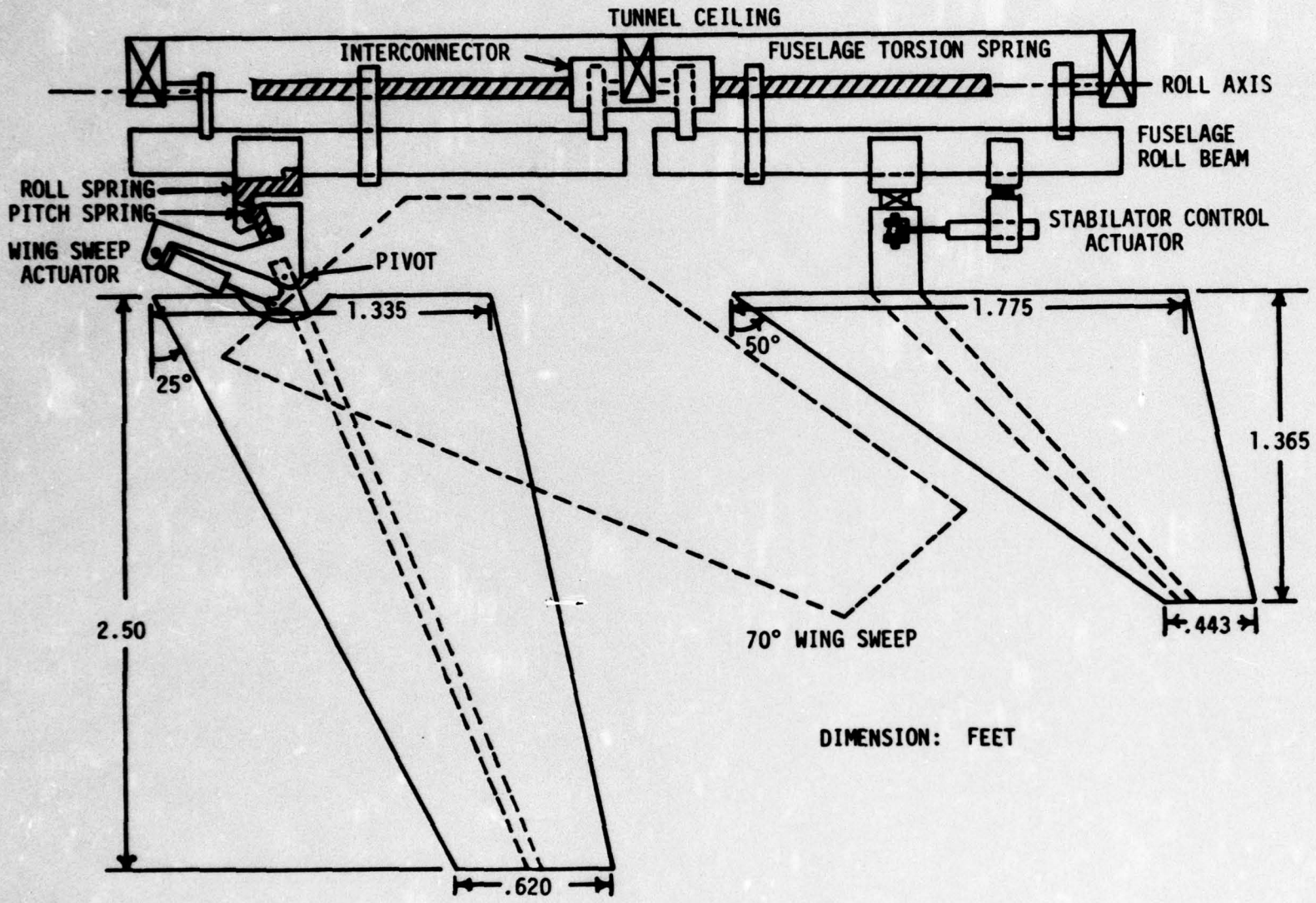

Figure 2. Schematic of Actively Controlled AFFDL Wing-Tail Flutter Model

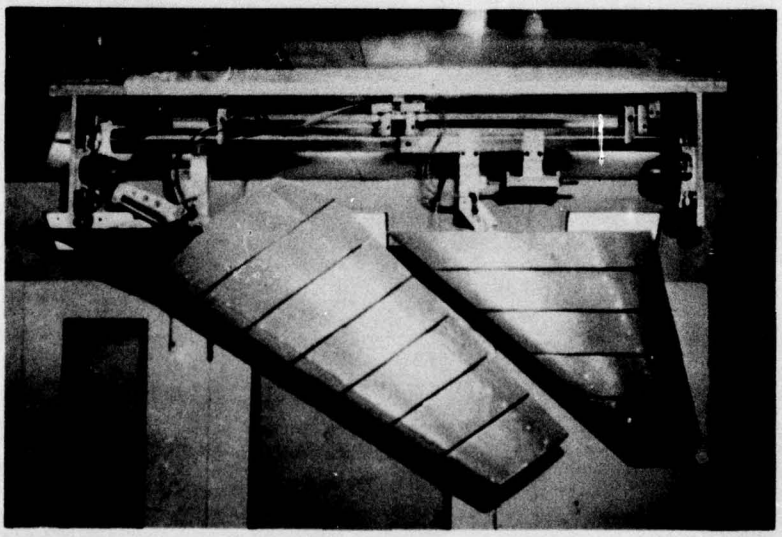

Figure 3. Installation of Modified AFFDL Wing-Tail Flutter Model in 7 Ft. by 10 Ft. Subsonic Wind Tunnel

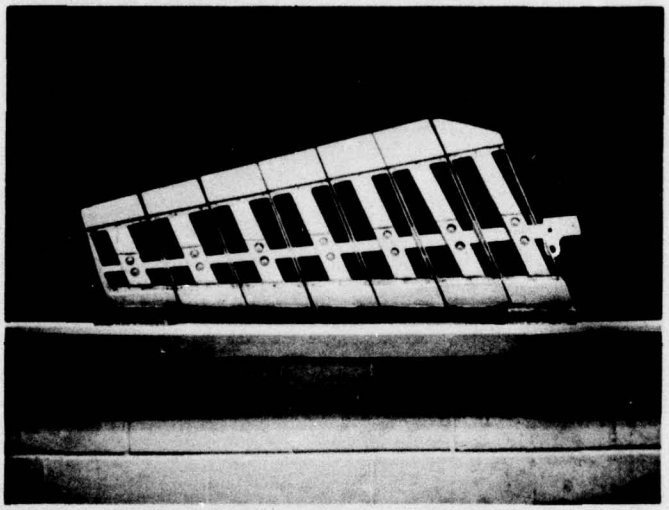

Figure 4. Wing Construction of AFFDL Model

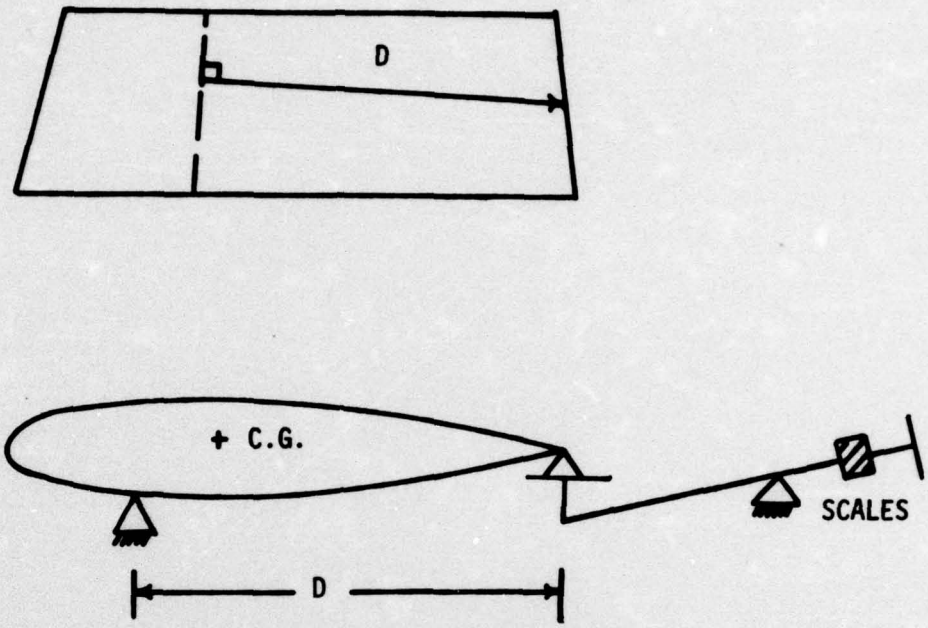

Figure 5. Schematic of Static Unbalance Measurements

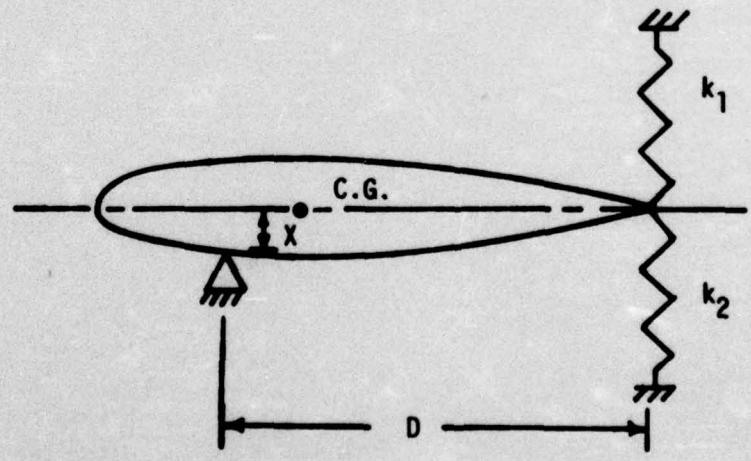

Figure 6. Schematic of Inertia Measurements

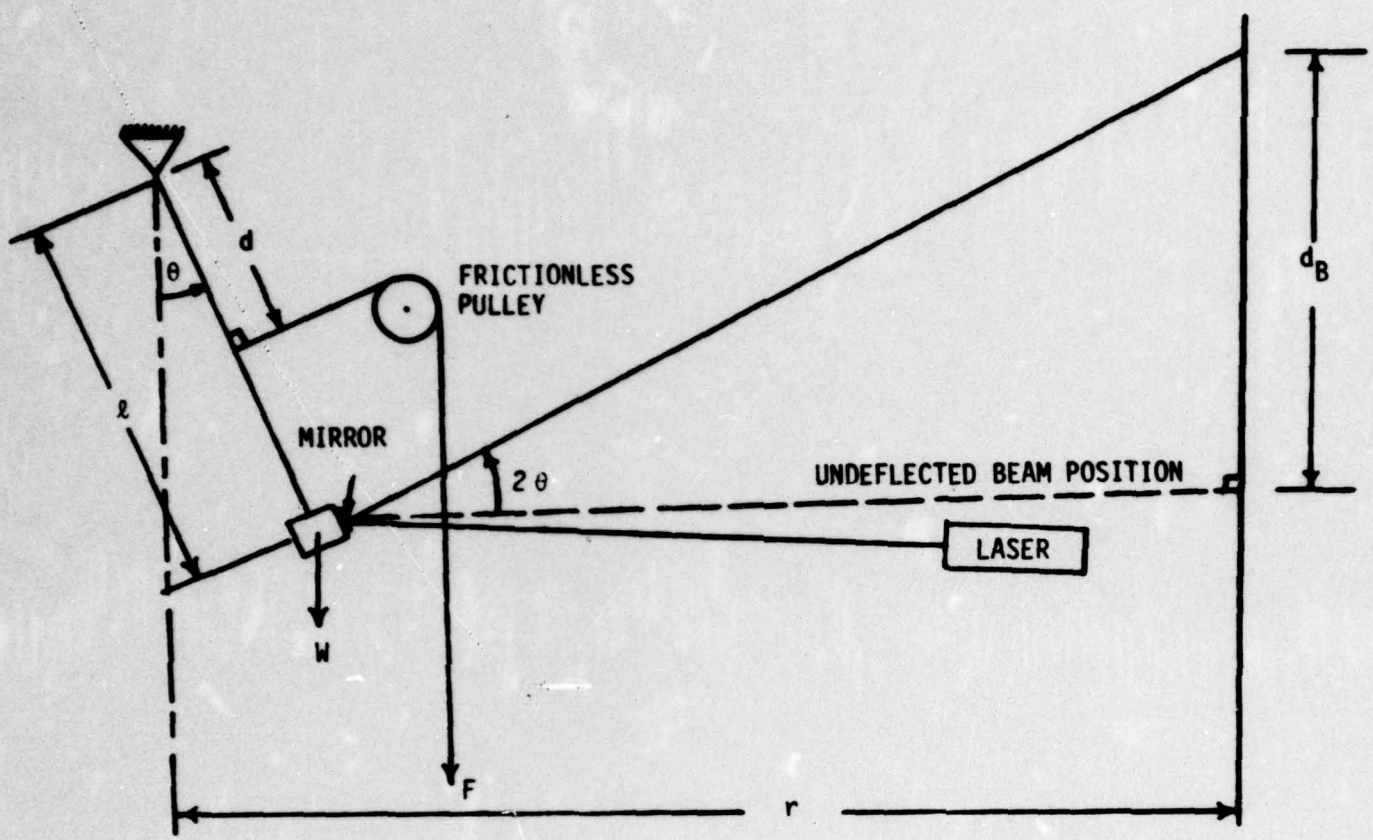

Figure 7. Schematic of Fuselage Roll Inertia Measurement

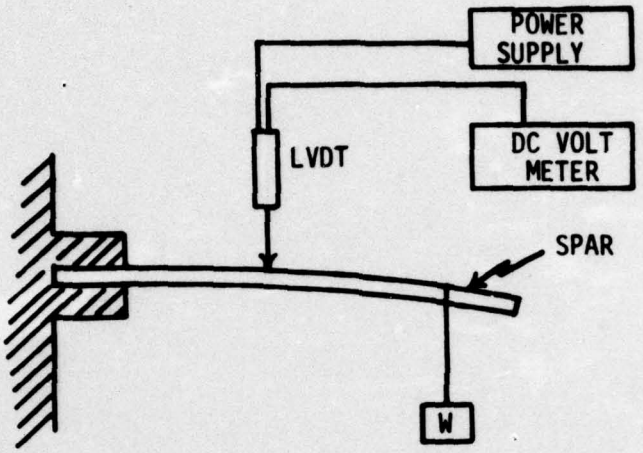

Figure 8. Schematic of Spar Bending Flexibility Measurement

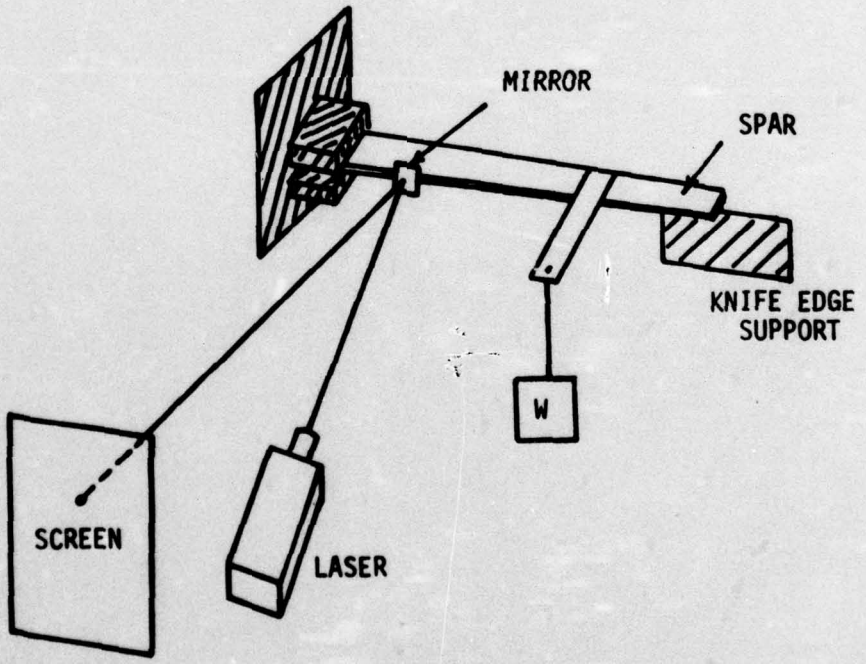

Figure 9. Schematic of Spar Torsional Flexibility Measurement

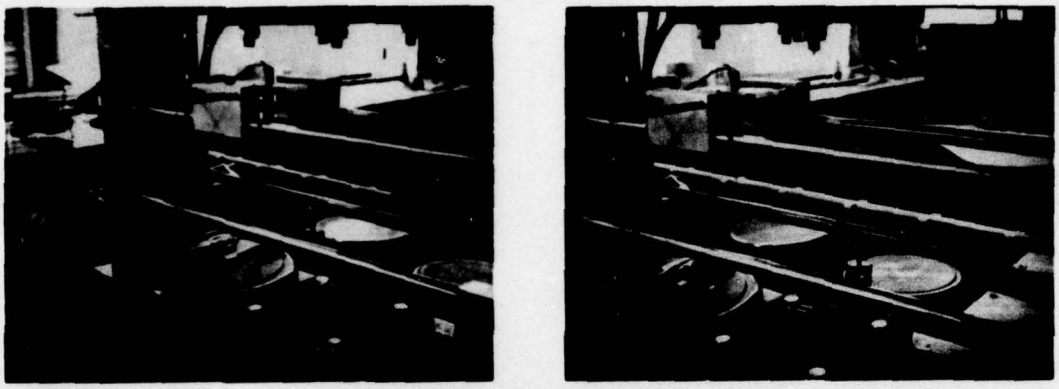

Figure 10. Measurement of Spar Bending Flexibility

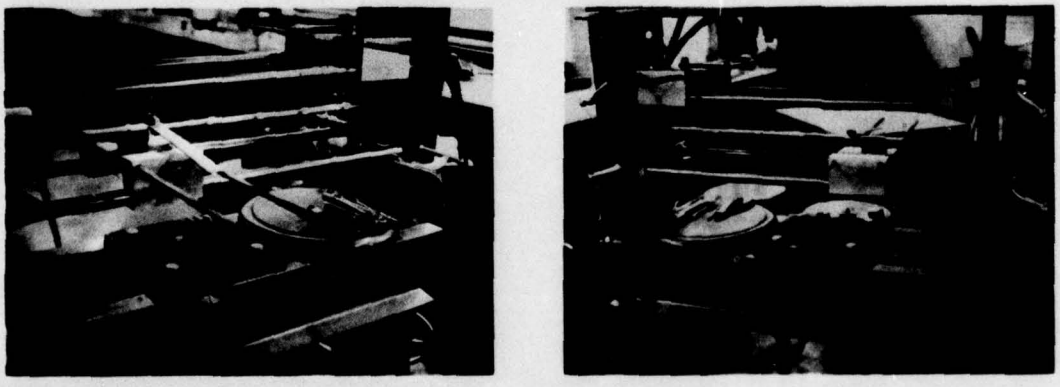

Figure 11. Measurement of Spar Torsional Flexibility

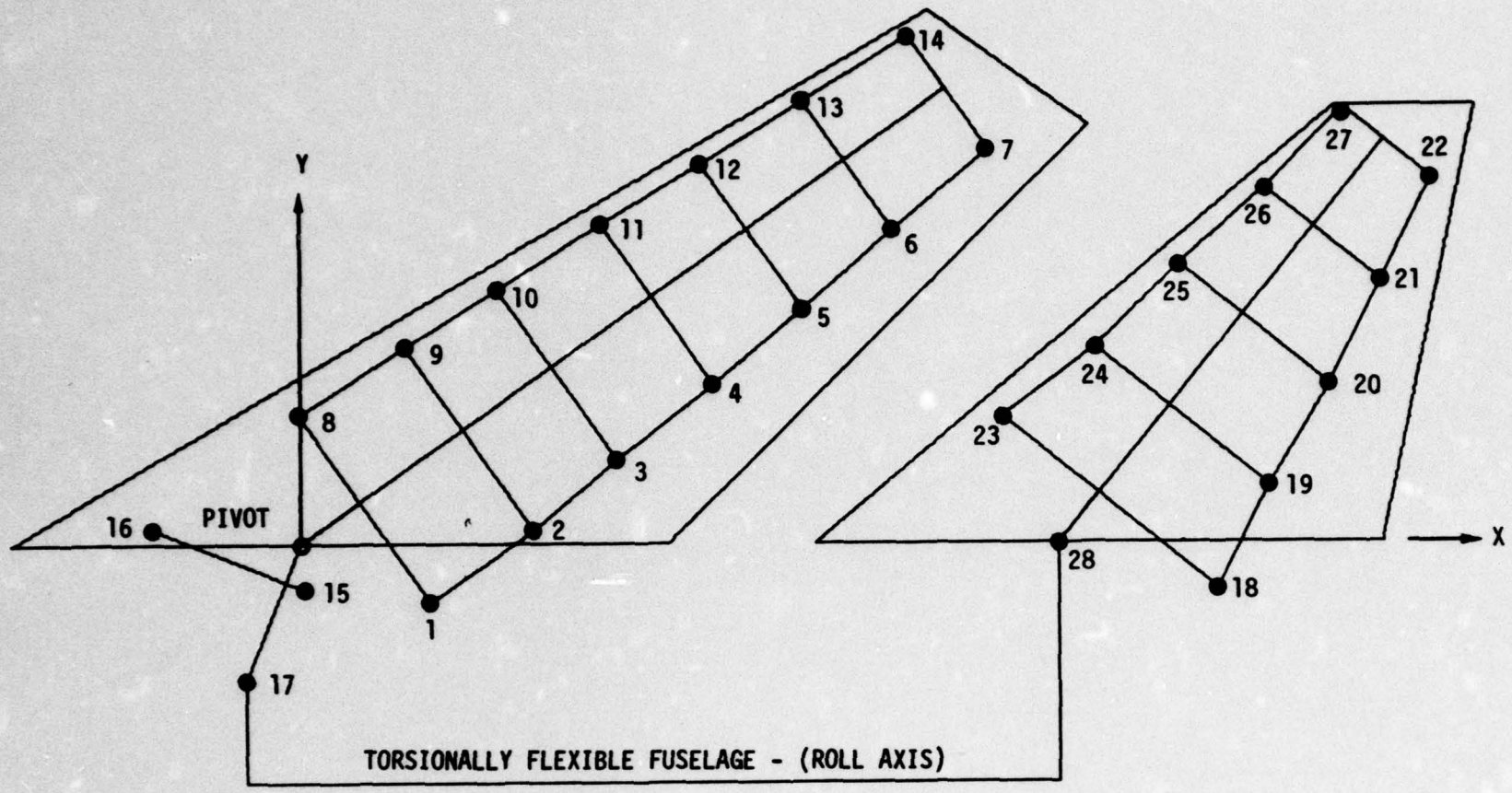

Figure 12. AFFDL 60° Dynamic Modeling

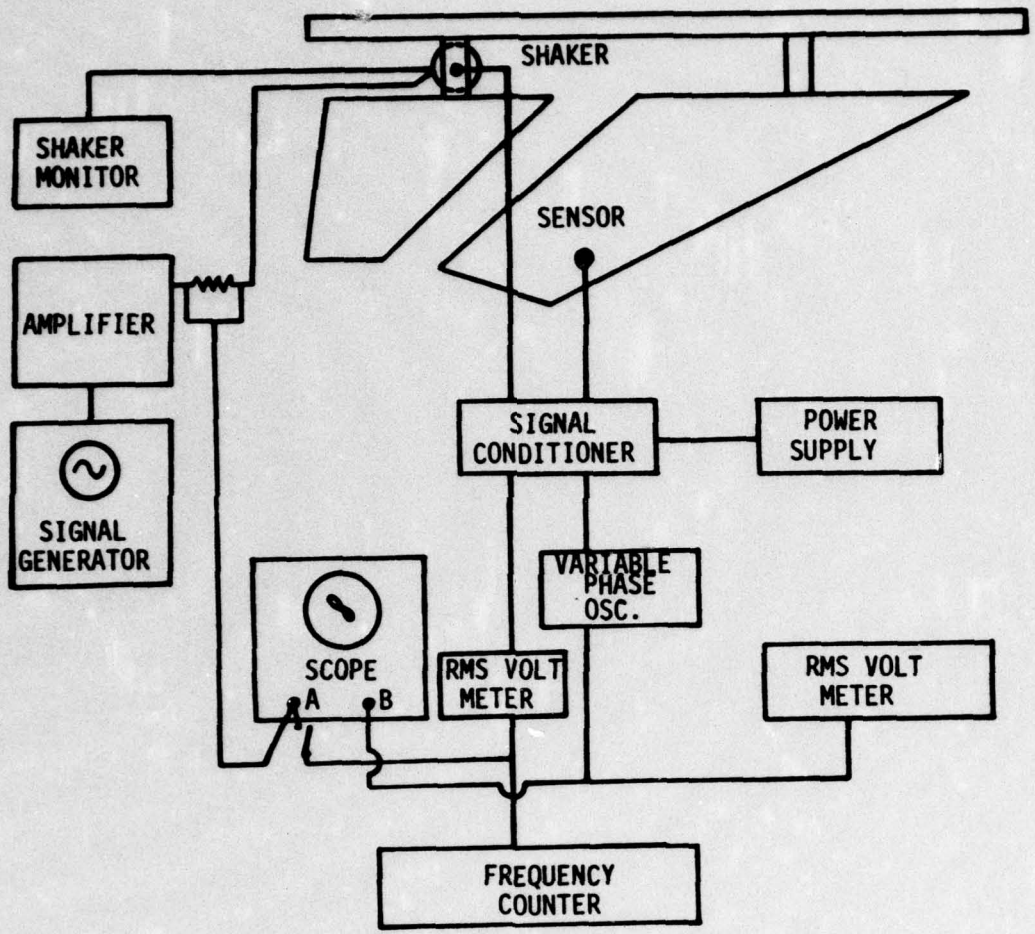

Figure 13. Schematic Diagram of Experimental Modeshape Measurement

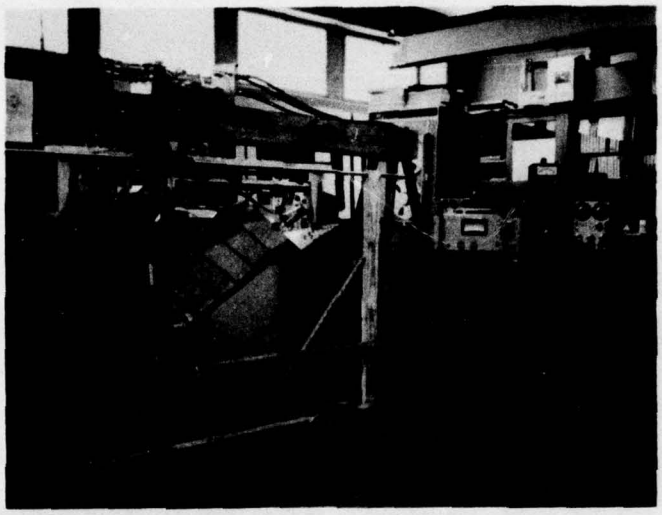

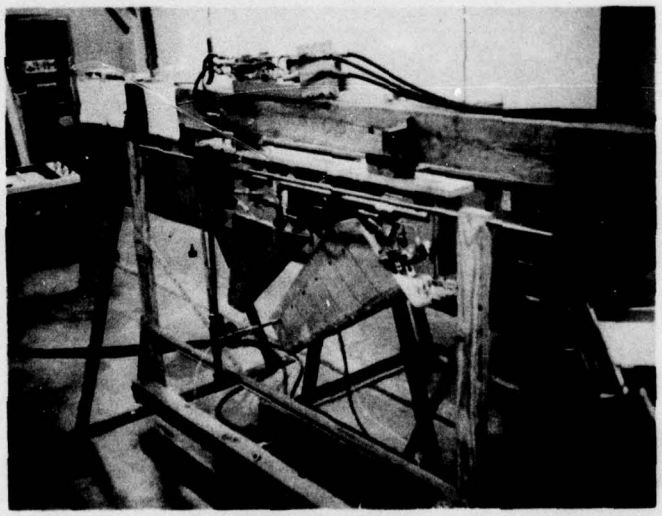

Figure 14. Experimental Modeshape Measurement Apparatus

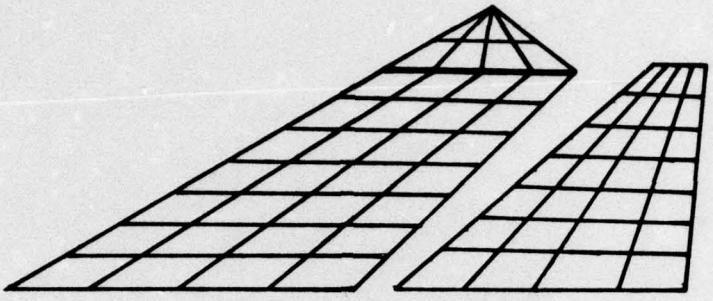

60° Sweep (64 boxes)

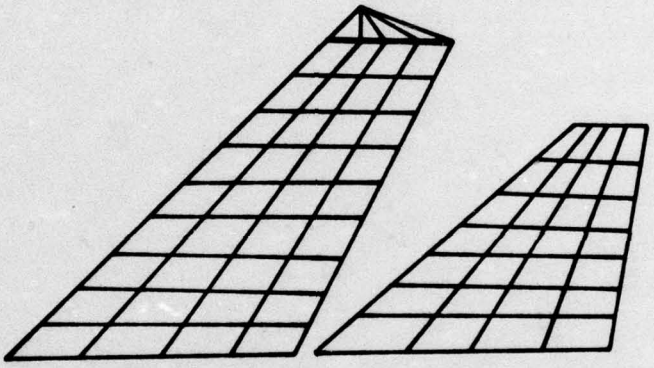

45° Sweep (68 boxes)

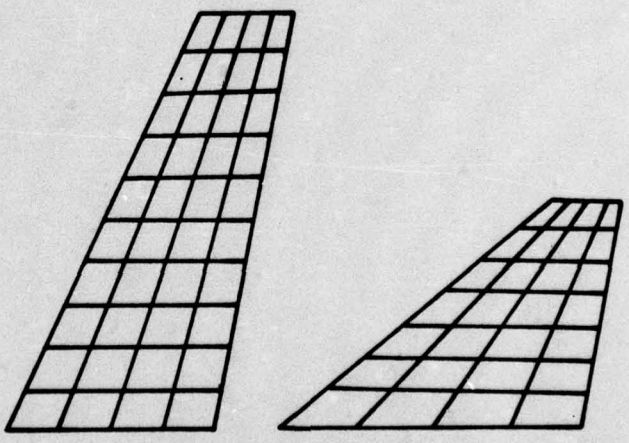

25° Sweep (68 boxes)

Figure 15. AFFDL Aerodynamic Modeling

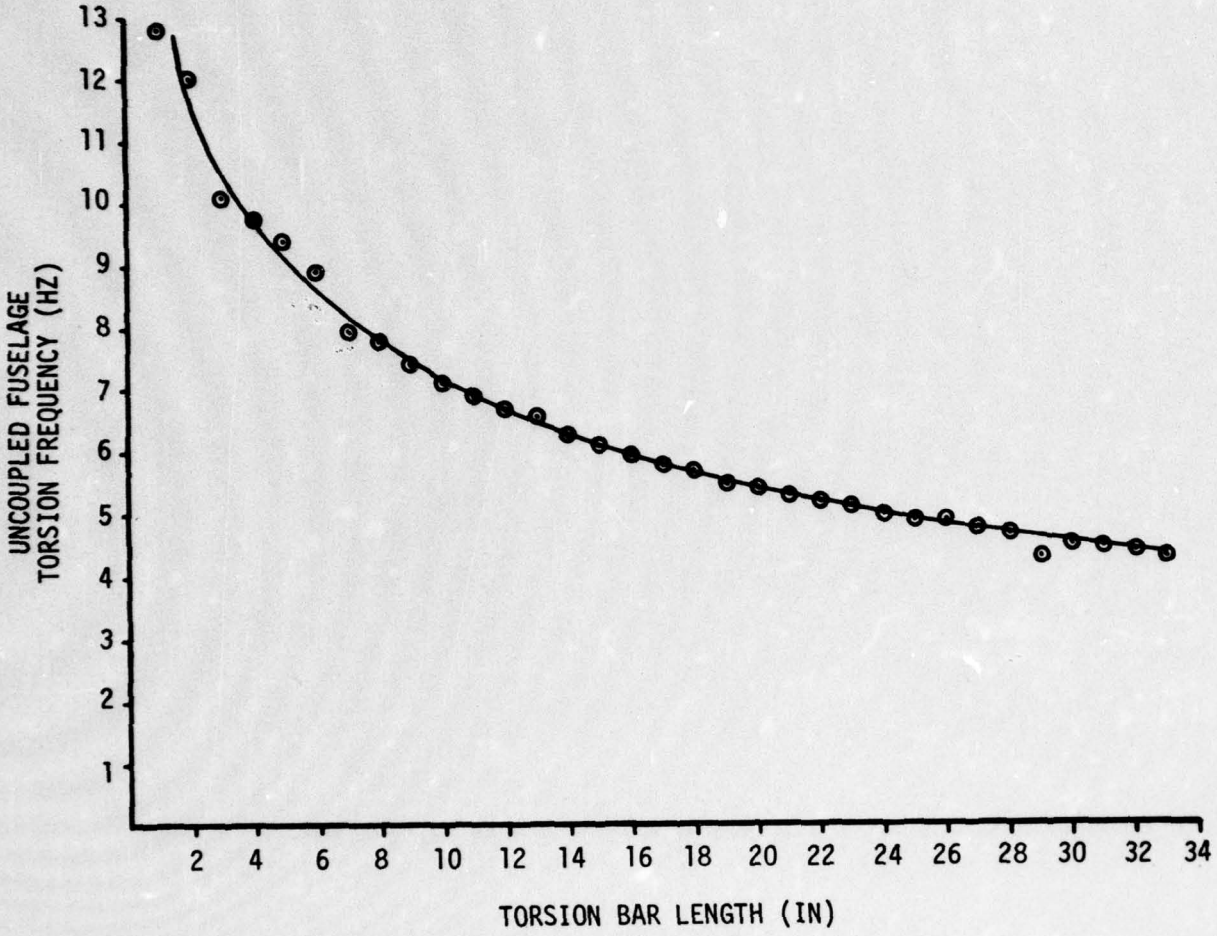

Figure 16. Uncoupled Fuselage Torsion Frequency vs. Torsion Bar Length, 25-Degree Sweep Angle

APPENDIX A

COMPUTATION OF NATURAL MODES AND FREQUENCIES FROM EXPERIMENTAL DATA

Several methods are available for calculating the generalized stiffness, K_{rs}, and generalized mass, m_{rs}, terms appearing in the flutter eigenvalue problem, Eq. (3.1). The following description outlines the method employed in this study to calculate the vibrational modes and frequencies used in the evaluation of these terms. Whenever possible, experimental measurements of mass, stiffness and inertia were utilized in the analysis so that the calculated natural vibration modes and frequencies would closely match those of the actual model. The following analysis procedure was incorporated into a computer code which would generate the lumped mass model from experimental data and then calculate the required modes, frequencies, and generalized masses for a fully flexible model. The computer code was designed such that variations in model mass or stiffness could be easily analyzed. In addition, the program was written so that it could be extended to the analysis of composite wing and tail spar configurations. All computations utilized the classical vibration and modeling techniques employed in structural dynamics and aeroelasticity.[14,15,16]

A.1 Lumped Mass Modeling from Experimental Inertia and Static Unbalance

Each wing and tail section was replaced by an equivalent dumbbell unit which contained equal concentrated mass at each end connected by a rigid, massless bar (see Fig. 12).[9] The bar was positioned perpendicular to the spar center line at the spanwise center of gravity location for the section. The bar lengths forward and aft of the spar center line were then calculated for each section such that section inertia and static unbalance were preserved. This calculation is shown in Eq. (A.1):

$$X_{for} = \frac{S}{M} - \sqrt{\frac{I_s}{M} - \left(\frac{S}{M}\right)^2}$$

$$X_{aft} = \frac{S}{M} + \sqrt{\frac{I_s}{M} - \left(\frac{S}{M}\right)^2} \qquad \text{(A.1)}$$

where

- S is the section static mass unbalance (slug-ft)
- I_s is the section inertia about the spar line (slug-ft^2)
- M is the total section mass (slugs).

The wing carry-through assembly was also modeled with a dumbbell unit since it was heavy and quite flexible.

Two additional concentrated mass points, 17 and 28, account for the experimental roll inertias of the forward and aft fuselage sections,

respectively (see Fig. 12). The locations of these nodes were chosen to give a useful structural deflection point and their mass values were then calculated to give the correct inertia about the roll axis.

A.2 Assembly of the Model Flexibility Matrix

The structural flexibility matrix used to compute the natural vibration modes is assembled from the experimentally measured uncoupled bending and torsional influence coefficients. The assembly procedure computes the deflection at a lumped mass point on the structure, due to a unit load at any other point, by summing the contributions due to spar bending, spar torsion, fuselage torsion, roll spring flexure, and pitch spring flexure. The moment arm lengths about the different torsional flexure axes are computed as a function of spar sweep angle. In this manner, the uncoupled flexibility influence coefficients of the model's elastic components can be easily measured experimentally and then assembled to obtain the entire system flexibility for any geometry.

It is implied in the assembly of a structural flexibility matrix that the structure is constrained at some point[12] to prevent the deflections from being unbounded, and in general, the constraint can be imposed at an arbitrary point on the structure.[16] The model in this study is constrained at mass point 28 on the tail spar rigid carry-through, allowing the fuselage torsional degree of freedom to provide for relative motion between wing and tail.

A.3 Solution for Vibration Modes of a Structure with Rigid Body Degrees of Freedom

Using the flexibility formulation, the free vibration modes of a constrained structure can be computed from

$$[\bar{K}]^{-1} [\bar{M}] \{h\}_r = \frac{1}{\omega_r^2} \{h\}_r \qquad (A.2)$$

where

$[\bar{M}]$	is the diagonal lumped mass matrix
$[\bar{K}]^{-1}$	is the flexibility matrix or inverted stiffness matrix
ω_r	is the natural frequency of the r^{th} mode
$\{h\}_r$	is the r^{th} mode shape or eigenvector.

Since the AFFDL model includes a rigid body roll degree of freedom, the mass matrix in Eq. (A.2) must be modified as shown in References 17 and 18 in order to obtain the free-to-roll, coupled, anti-symmetric modes of the entire model. This modification involves pre- and post- multiplying the lumped mass matrix by a constraining matrix, [C], which preserves angular momentum about the model roll axis. The constrained mass matrix is defined as

$$[M'] = [C]^T [\bar{M}] [C] \ . \qquad (A.3)$$

For the case of rigid body roll, the constraint matrix is defined by:

$$[C] = [I] - \frac{1}{I_R} \{y\} \{y\}^T [\bar{M}] \tag{A.4}$$

where

$[I]$ is the identity matrix,

I_R is the total mass moment of inertia of the structure about its rigid body rotation axis,

$\{y\}$ is a vector of displacements of the structural mass points due to a unit rigid-body motion. (Assuming linearized theory and using a unit rotation, this vector is the vector of distances of the mass points from the rigid body roll axis.)

The constrained mass matrix, $[M']$, is now used with the constrained flexibility matrix, described in Section A.2, to solve for the relative motion vibrational modes. (The absolute motion of the flexible structure in any mode can be obtained by adding the proper rigid body component to the relative motion as shown in Reference 18.) Substituting $[M']$ for $[\bar{M}]$ in Eq. (A.2) gives the following eigenvalue problem which can be solved for the relative motion flexible modes:

$$[\bar{K}]^{-1} [C]^T [\bar{M}] [C] \{h_R\}_r = \frac{1}{\omega_r^2} \{h_R\}_r \tag{A.5}$$

After obtaining the relative flexible modes, $\{h_R\}$, they are transformed back to the absolute (free-free) modes by

$$\{h_A\}_r = [C]\{h_R\}_r \tag{A.6}$$

as shown in Reference 17.

The solution of Eq. (A.5) for the AFFDL model involved only 27 degrees of freedom since the 28th point was constrained. The [C] matrix was computed with dimensions of 28 x 28, but the 28th column is dropped during the calculation of Eq. (A.3) in order to reduce out the mass at the constrained point (I.E., [C] is used as a 28 x 27 matrix). The entire 28 x 28 [C] matrix is used in Eq. (A.6) to transform from the relative to the absolute modeshapes.

The rigid body mode, which is a gravitational pendulum mode, can now be calculated from one of the relative flexible modes by the method given in Reference 18. In matrix form, this calculation can be written as

$$\{h_A\}_{rigid} = \{y\} \cdot \phi_R \tag{A.7}$$

where

ϕ_R is a scalar representing the value of the rigid body coordinate (in this case a rotation angle).

The rigid body component, ϕ_R, can be expressed as

$$\phi_R = -\frac{1}{I_R} \{y\}^T [\bar{M}] \{h_R\} \tag{A.8}$$

where

$\{h_R\}$ is any one of the previously determined relative flexible modes

After combining Eq. (A.7) with Eq. (A.8), the rigid pendulum mode is calculated from

$$\{h_A\}_{rigid} = -\frac{1}{I_R} \{y\} \{y\}^T [\bar{M}] \{h_r\} \tag{A.9}$$

Eq. (A.9) is recognized as the second expression of the constraining equation, Eq. (A.4), multiplied by a flexible modeshape. The first flexible mode is used in this study since it is determined with the greatest computational accuracy.

The complete set of free-free vibration modes is now normalized so that each modeshape vector has unity magnitude. It should also be mentioned at this point that the solution procedure insures that the flexible modes are orthogonal to each other with respect to the lumped mass matrix, $[\bar{M}]$. Additional orthogonality conditions between the rigid body mode and the flexible modes are also satisfied.[11,14]

Now, the generalized mass can be computed from the absolute modes of Eqs. (A.6) and (A.9) by

$$m_{rs} = \{h_A\}^T_r [\bar{M}] \{h_A\}_s$$

where

$\{h_A\}_s$ is the vector of displacements of the s^{th} absolute mode

$\{h_A\}^T_r$ is the transpose of the vector of displacements of the r^{th} absolute mode.

Because of the orthogonality condition of the natural modes with respect to the lumped mass matrix

$$m_{rs} = 0 \qquad \text{for } r \neq s \ .$$

The generalized stiffness, K_{rs}, is then determined from

$$K_{rr} = \omega_r^2 m_{rr} \ .$$

APPENDIX B

NATURAL VIBRATION MODES†

† For abbreviations and symbols, reference Table VIII.

AFFDL 60° Modeshapes , $\frac{\omega_h}{\omega_\theta} = 0.8$

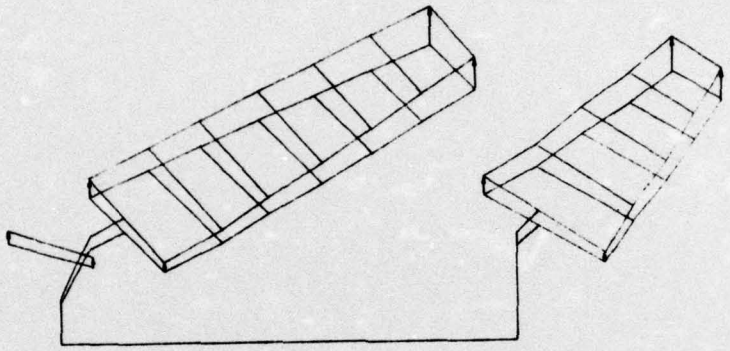

Pendulum Mode $\omega = 0.87$ Hz

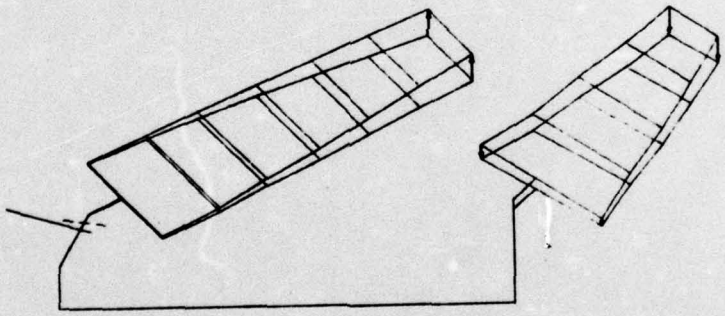

Mode 2 $\omega = 3.7$ Hz

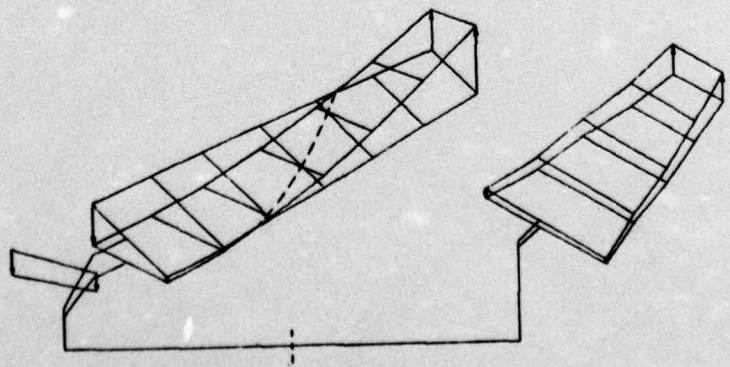

Mode 3 $\omega = 8.1$ Hz

AFFDL 60° Modeshapes , $\frac{\omega_h}{\omega_\theta} = 0.8$

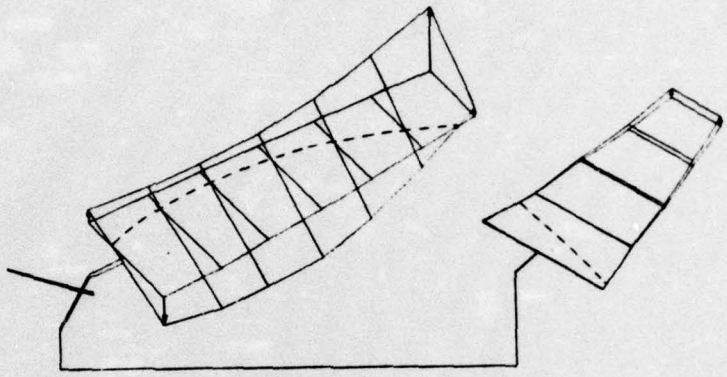

Mode 4 ω = 14.2 Hz

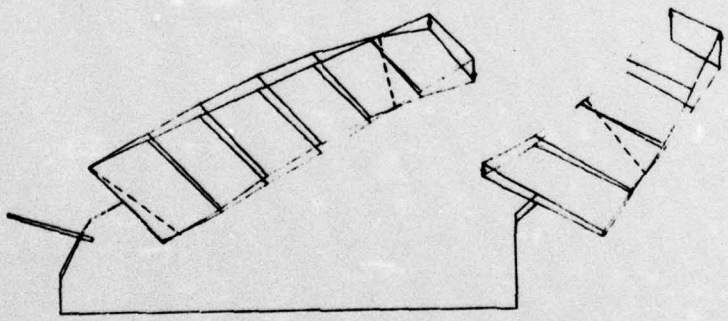

Mode 5 ω = 19.0 Hz

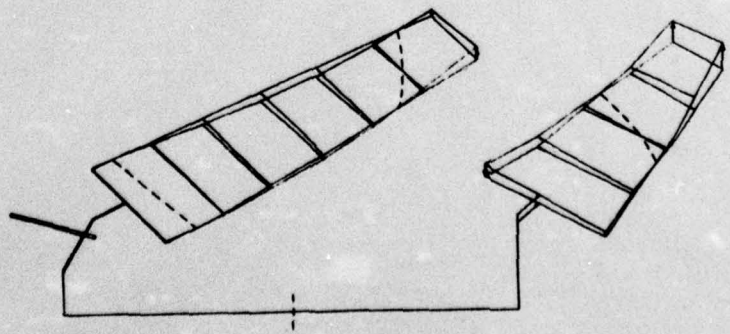

Mode 6 ω = 21.5 Hz

AFFDL 60° Modeshapes , $\frac{\omega_h}{\omega_\theta} = 0.6$

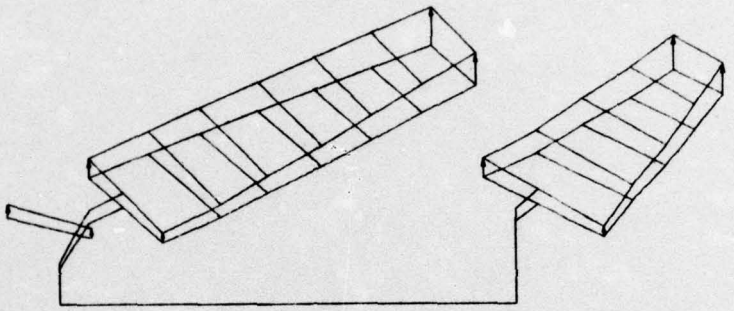

Pendulum Mode $\omega = 0.87$ Hz

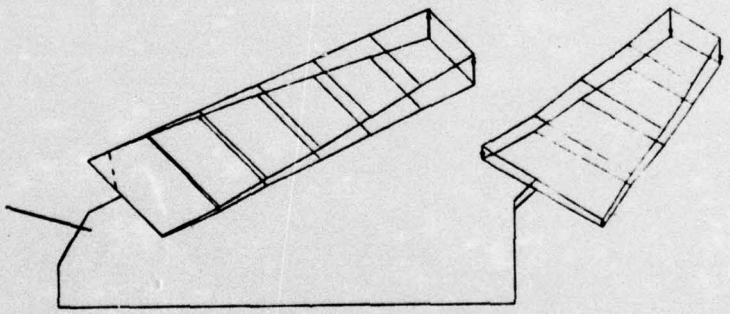

Mode 2 $\omega = 4.0$ Hz

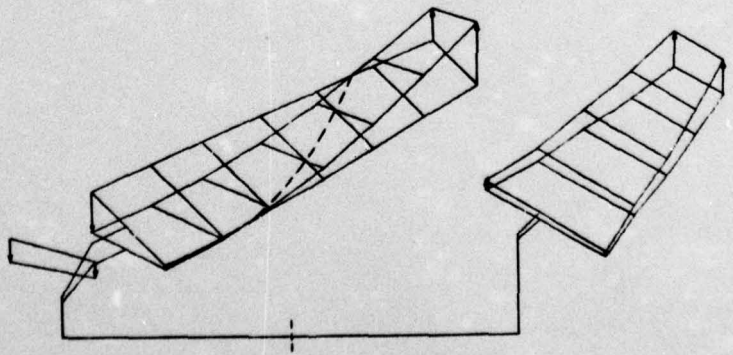

Mode 3 $\omega = 8.8$ Hz

AFFDL 60° Modeshapes , $\frac{\omega_h}{\omega_\theta} = 0.6$

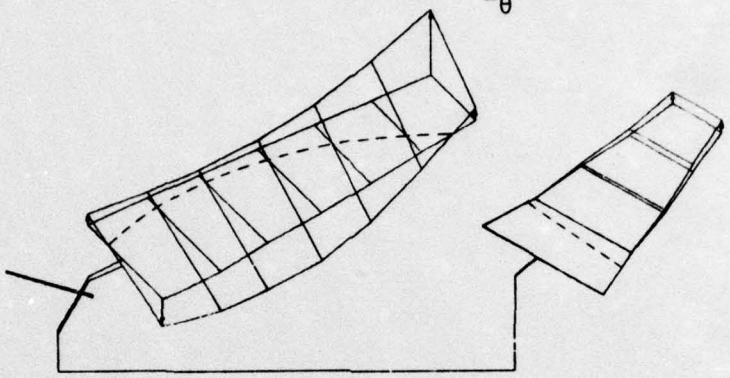

Mode 4 ω = 14.3 Hz

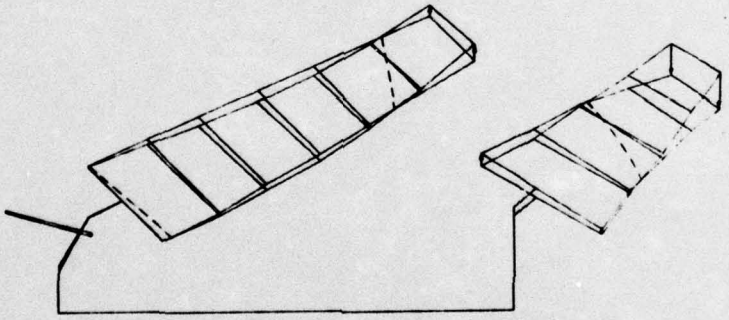

Mode 5 ω = 19.2 Hz

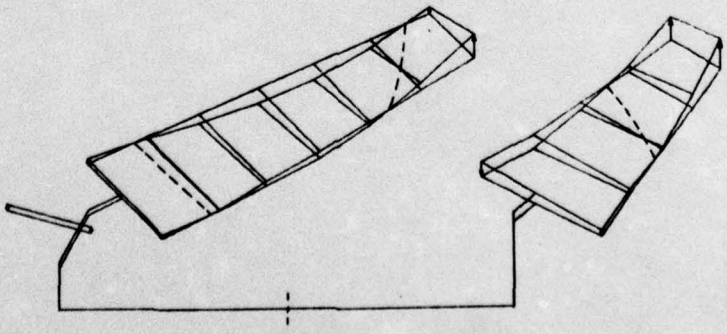

Mode 6 ω = 23.2 Hz

AFFDL 60° Modeshapes , $\frac{\omega_h}{\omega_\theta} = 0.4$

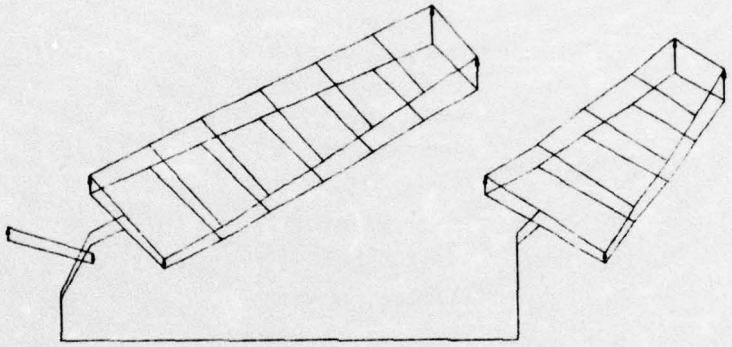

Pendulum Mode $\omega = 0.87$ Hz

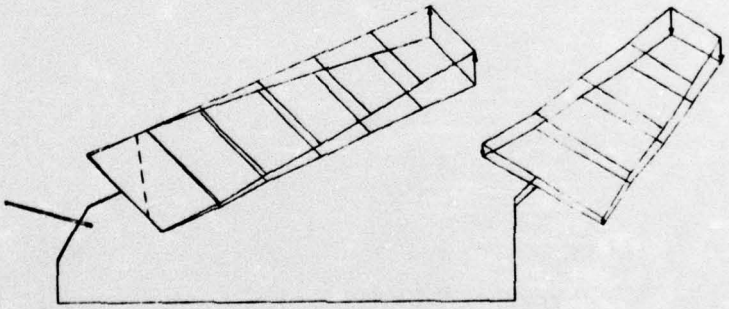

Mode 2 $\omega = 4.3$ Hz

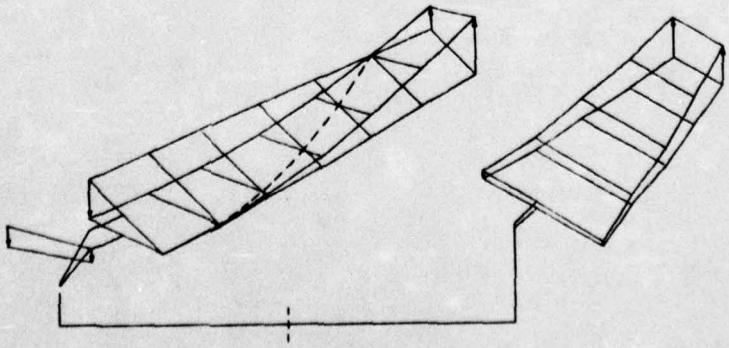

Mode 3 $\omega = 9.8$ Hz

AFFDL 60° Modeshapes , $\frac{\omega_h}{\omega_\theta} = 0.4$

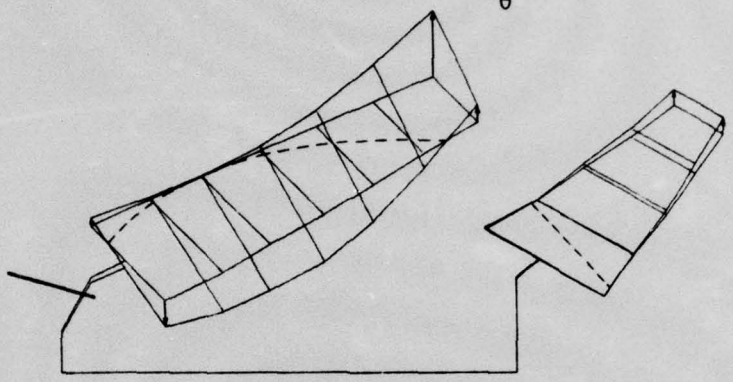

Mode 4 ω = 14.4 Hz

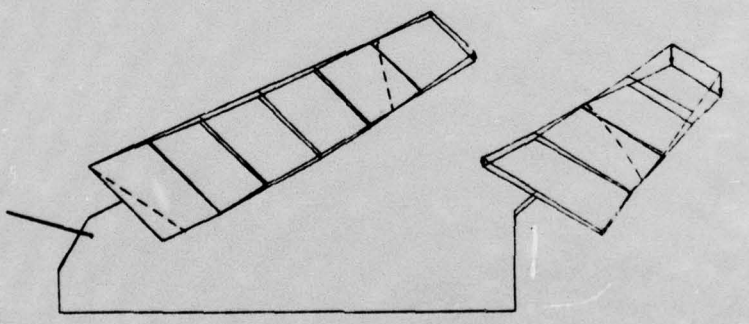

Mode 5 ω = 19.2 Hz

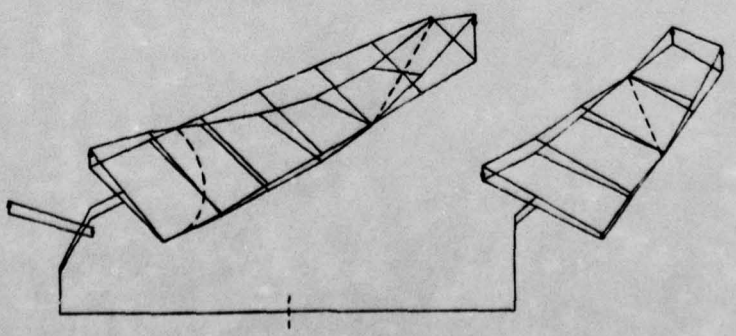

Mode 6 ω = 26.5 Hz

AFFDL 60° Modeshapes , $\frac{\omega_h}{\omega_\theta} = 0.6$, PM

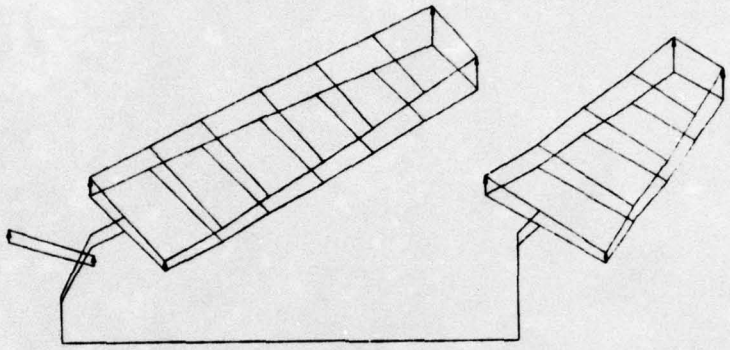

Pendulum Mode $\omega = 0.84$ Hz

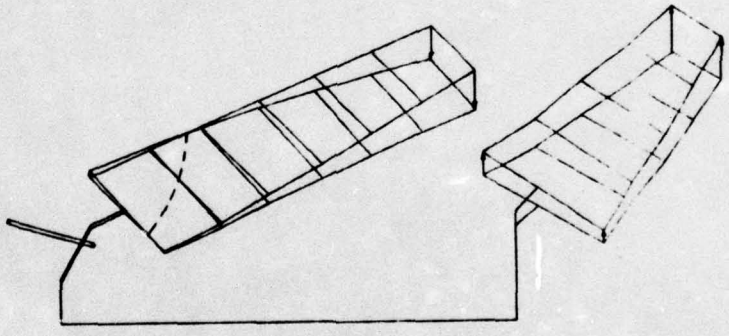

Mode 2 $\omega = 3.2$ Hz

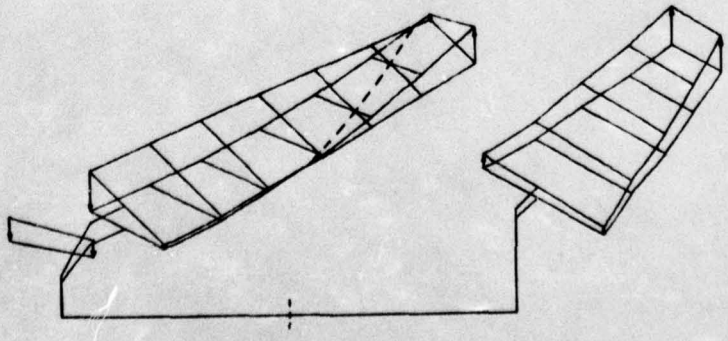

Mode 3 $\omega = 7.0$ Hz

AFFDL 60° Modeshapes , $\frac{\omega_h}{\omega_\theta} = 0.6$, PM

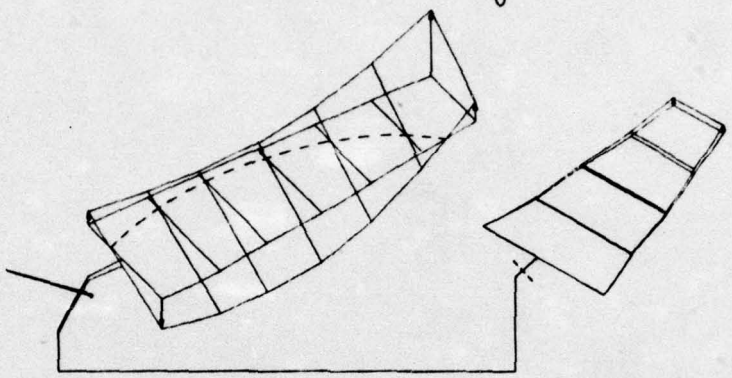

Mode 4 ω = 12.9 Hz

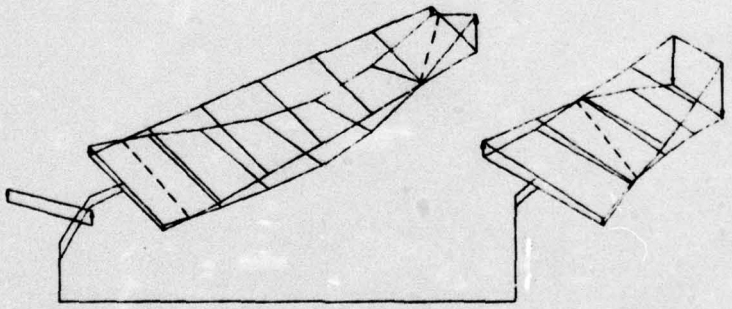

Mode 5 ω = 17.8 Hz

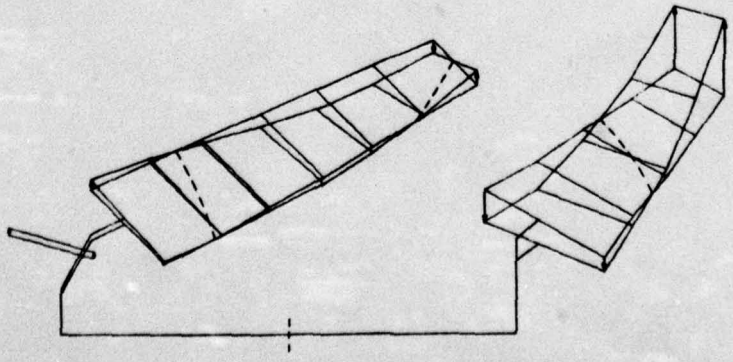

Mode 6 ω = 21.0 Hz

AFFDL 45° Modeshapes , *

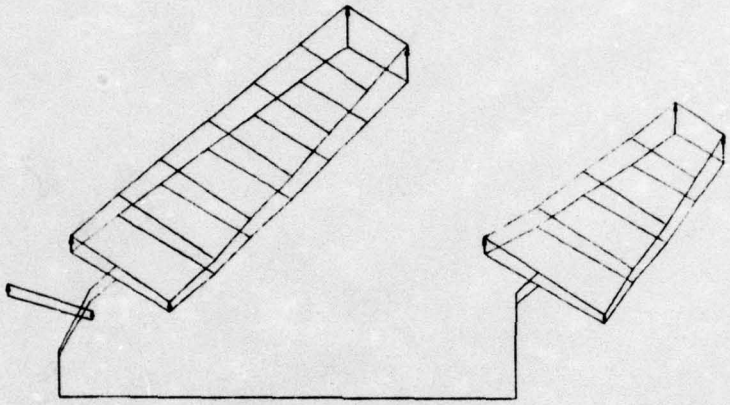

Pendulum Mode ω = 0.84 Hz

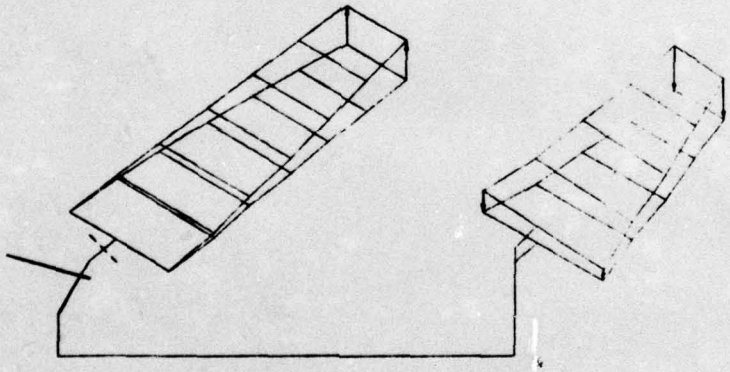

Mode 2 ω = 4.1 Hz

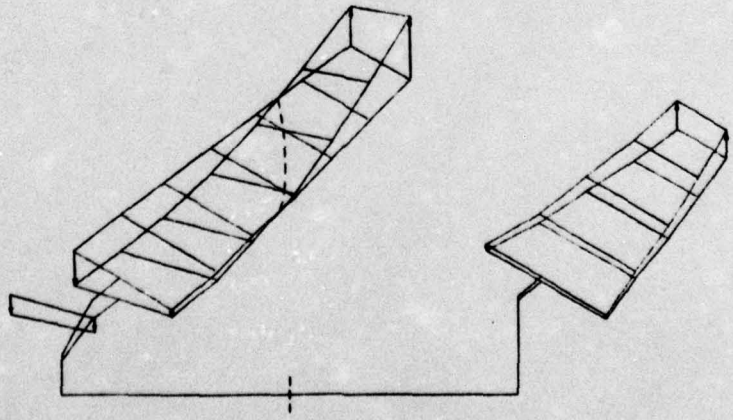

Mode 3 ω = 9.7 Hz

AFFDL 45° Modeshapes , *

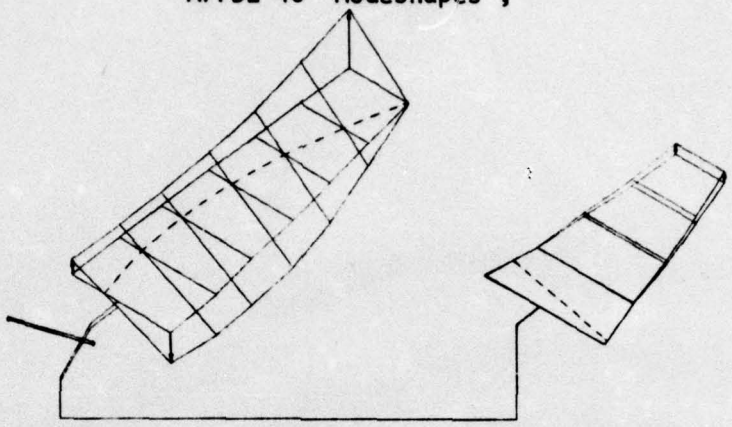

Mode 4 ω = 13.9 Hz

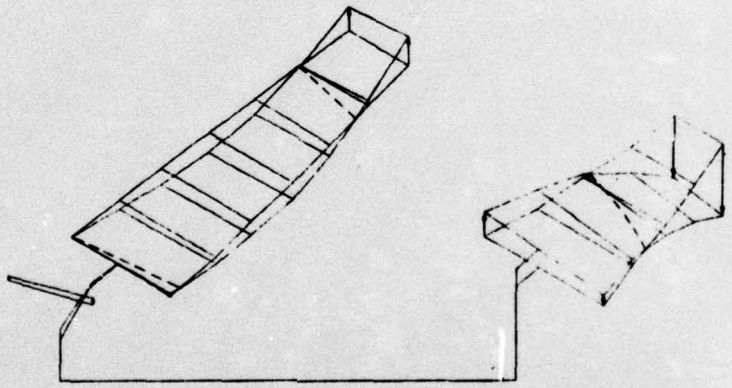

Mode 5 ω = 19.2 Hz

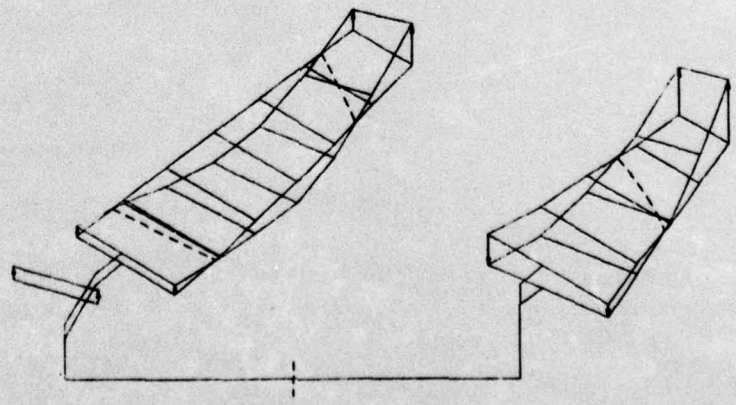

Mode 6 ω = 23.3 Hz

AFFDL 45° Modeshapes , # , PM

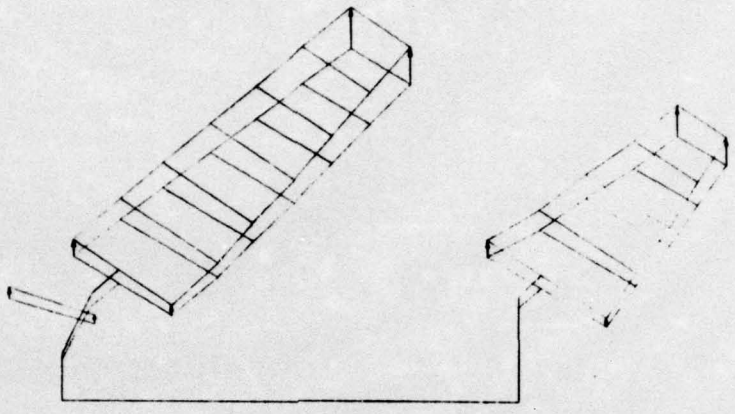

Pendulum Mode ω = 0.80 Hz

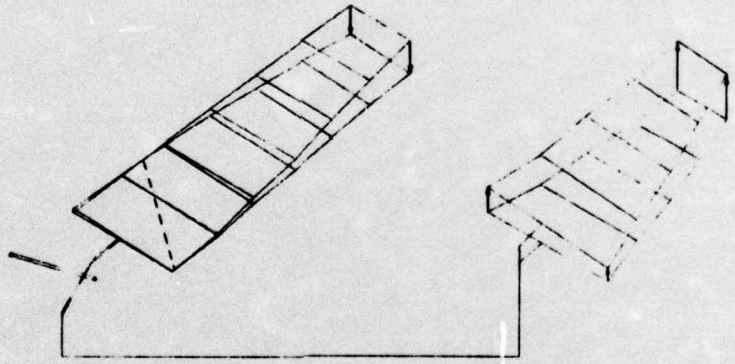

Mode 2 ω = 3.4 Hz

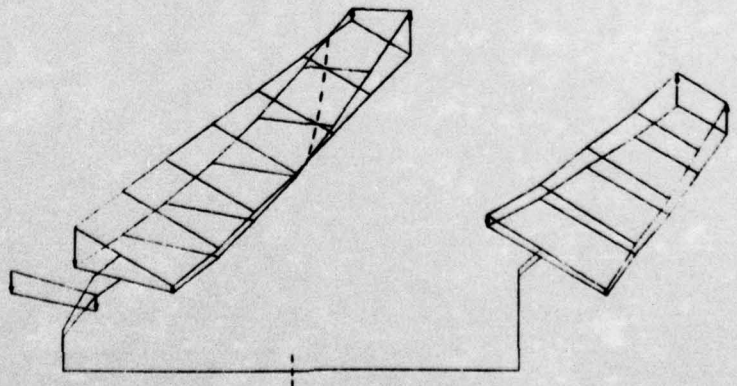

Mode 3 ω = 7.7 Hz

AFFDL 45° Modeshapes , # , PM

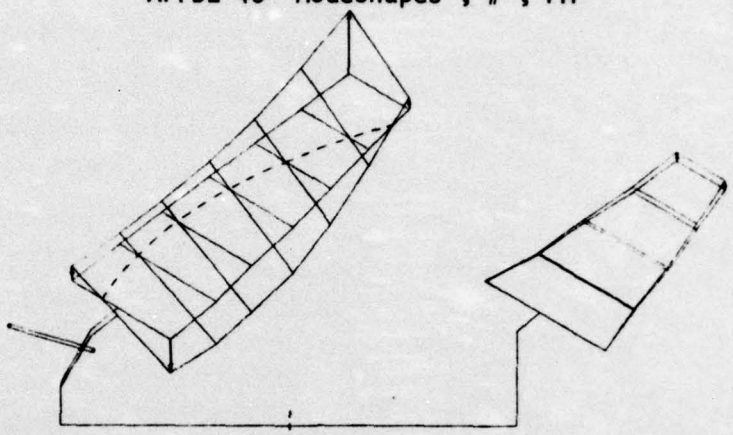

Mode 4 ω = 12.3 Hz

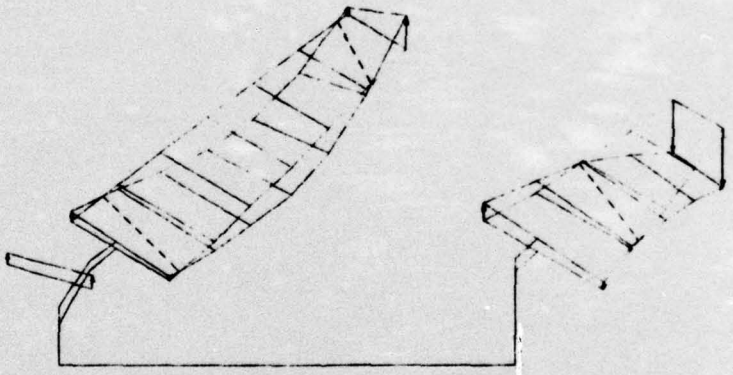

Mode 5 ω = 18.0 Hz

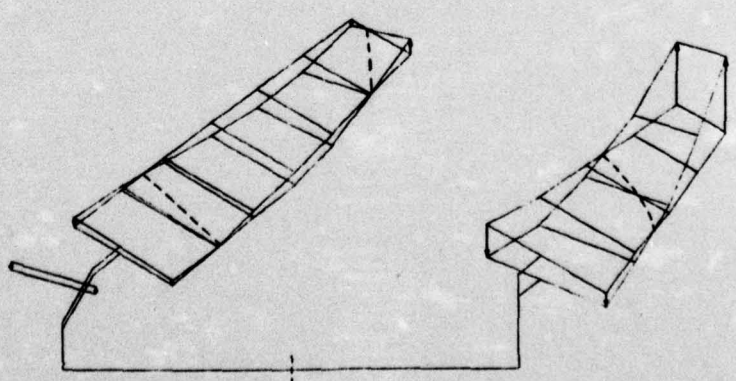

Mode 6 ω = 21.2 Hz

AFFDL 25° Modeshapes , *

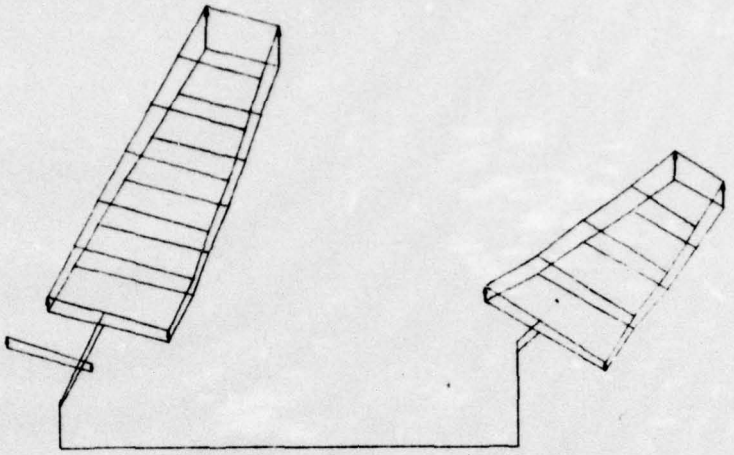

Pendulum Mode ω = 0.78 Hz

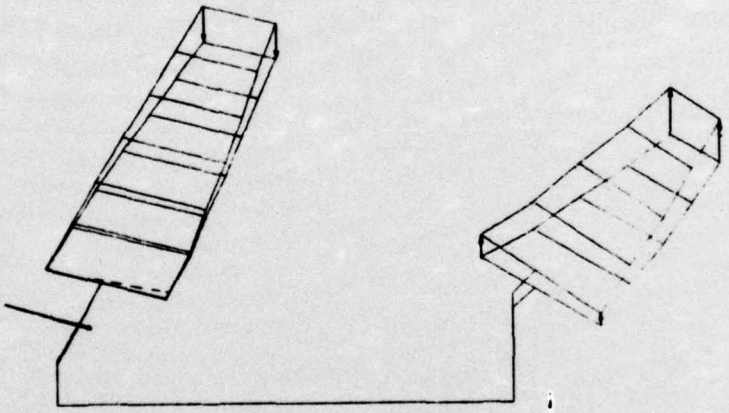

Mode 2 ω = 4.1 Hz

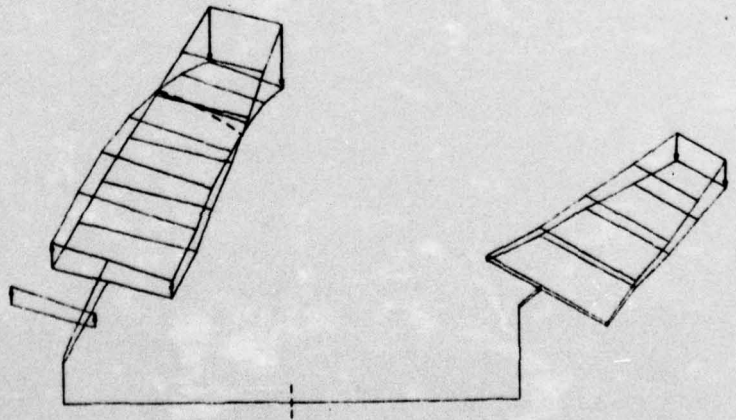

Mode 3 ω = 10.4 Hz

AFFDL 25° Modeshapes , *

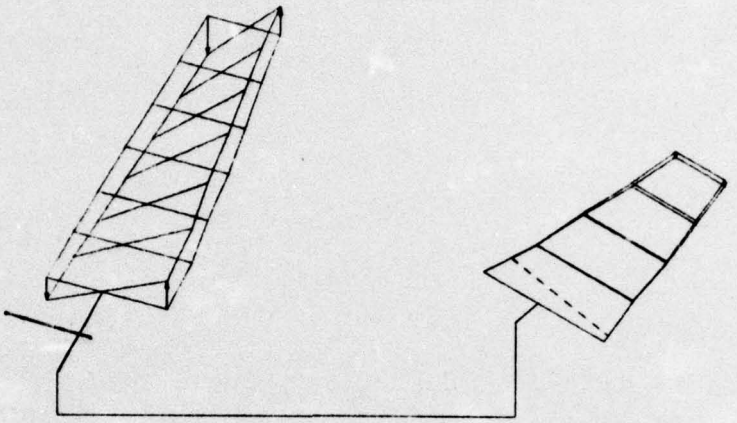

Mode 4 ω = 13.8 Hz

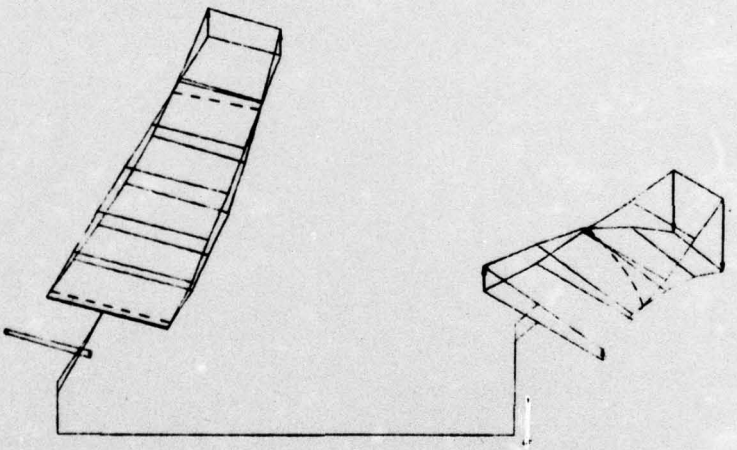

Mode 5 ω = 19.1 Hz

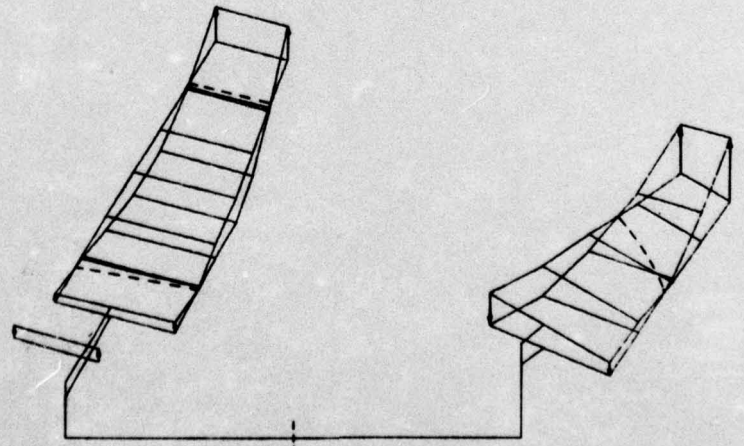

Mode 6 ω = 23.4 Hz

AFFDL 25° Modeshapes , # , PM

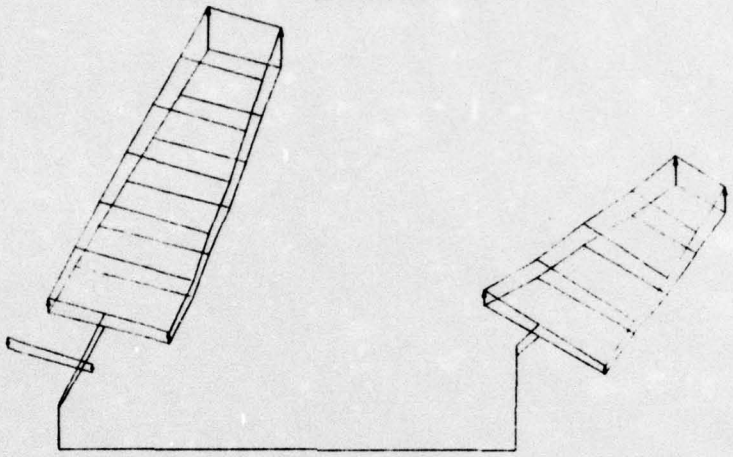

Pendulum Mode ω = 0.73 Hz

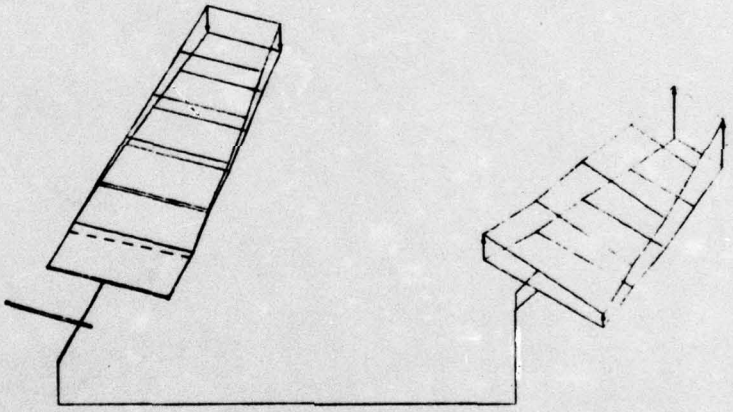

Mode 2 ω = 3.5 Hz

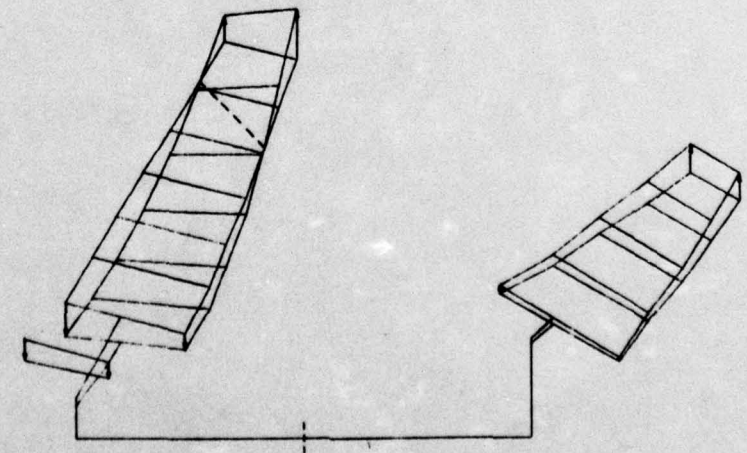

Mode 3 ω = 8.5 Hz

AFFDL 25° Modeshapes , #, PM

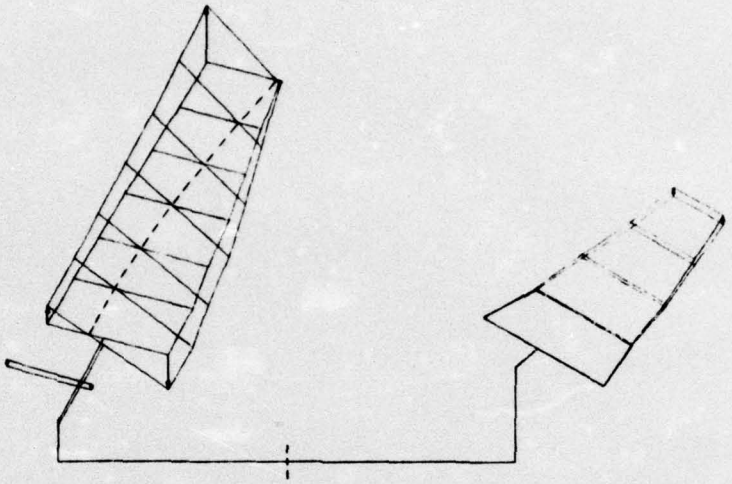

Mode 4 ω = 11.8 Hz

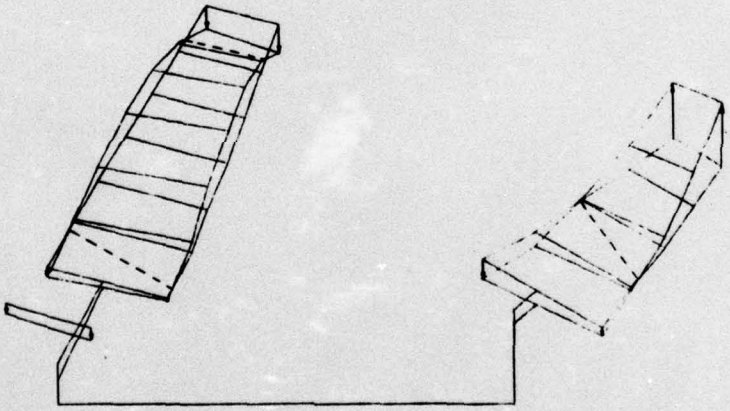

Mode 5 ω = 18.3 Hz

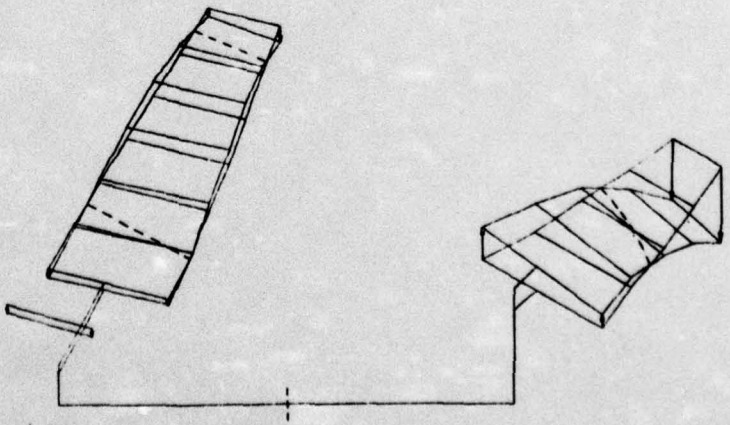

Mode 6 ω = 21.3 Hz

APPENDIX C

EXPERIMENTAL VIBRATION MODES

AFFDL 60° Experimental Modeshapes , $\frac{\omega_h}{\omega_\theta} = 0.6$

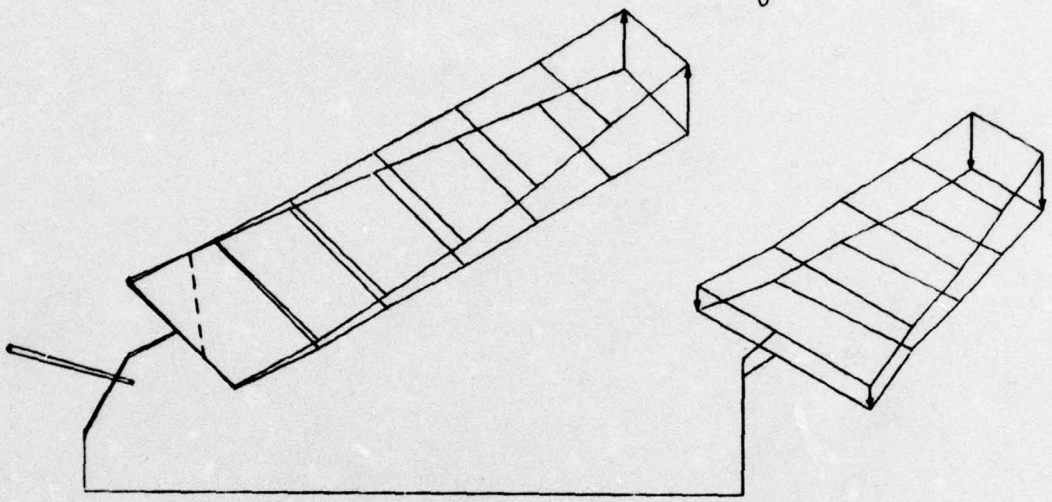

Mode 2 $\omega = 4.2$ Hz

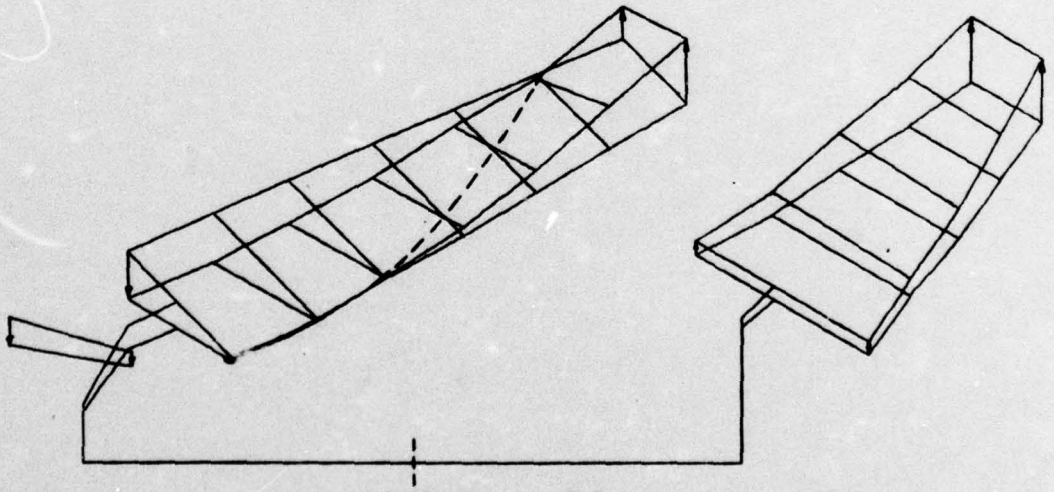

Mode 3 $\omega = 9.0$ Hz

AFFDL 60° Experimental Modeshapes , $\frac{\omega_h}{\omega_\theta} = 0.6$

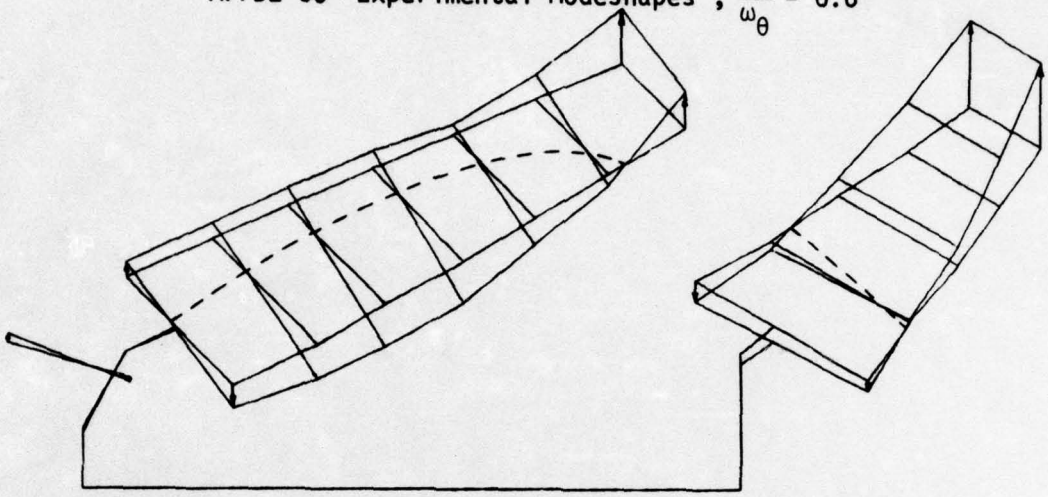

Mode 4 ω = 15.1 Hz

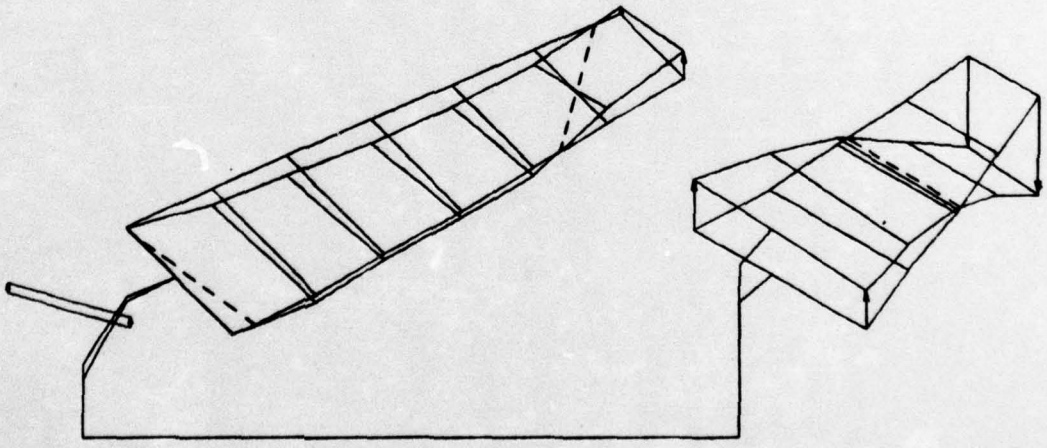

Mode 5 ω = 19.2 Hz

APPENDIX D

PLOTS OF DAMPING VS. VELOCITY AND FREQUENCY VS. VELOCITY†

† For abbreviations and symbols, reference Table XV.

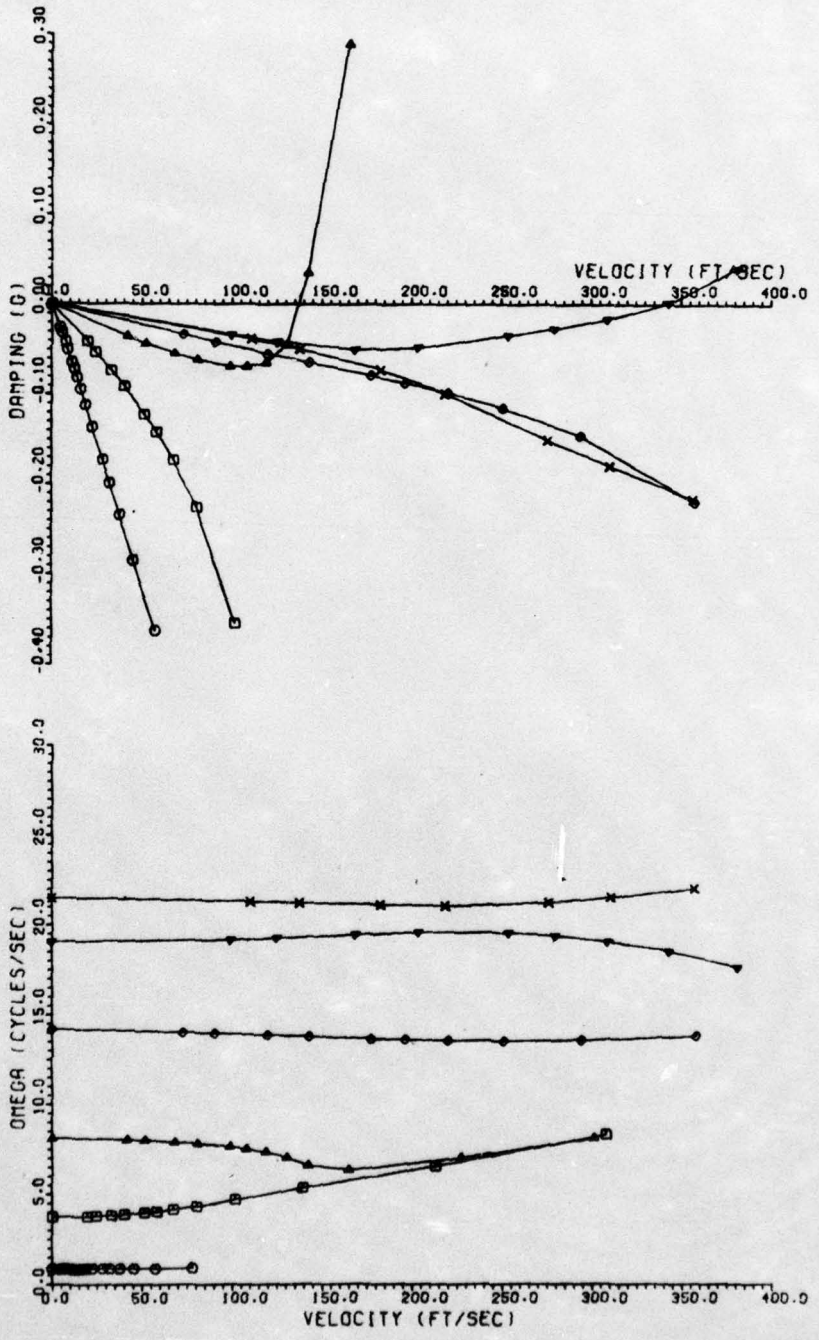

AFFDL 60° , $\frac{\omega_h}{\omega_\theta} = 0.8$, $\bar{X} = .25$ FT

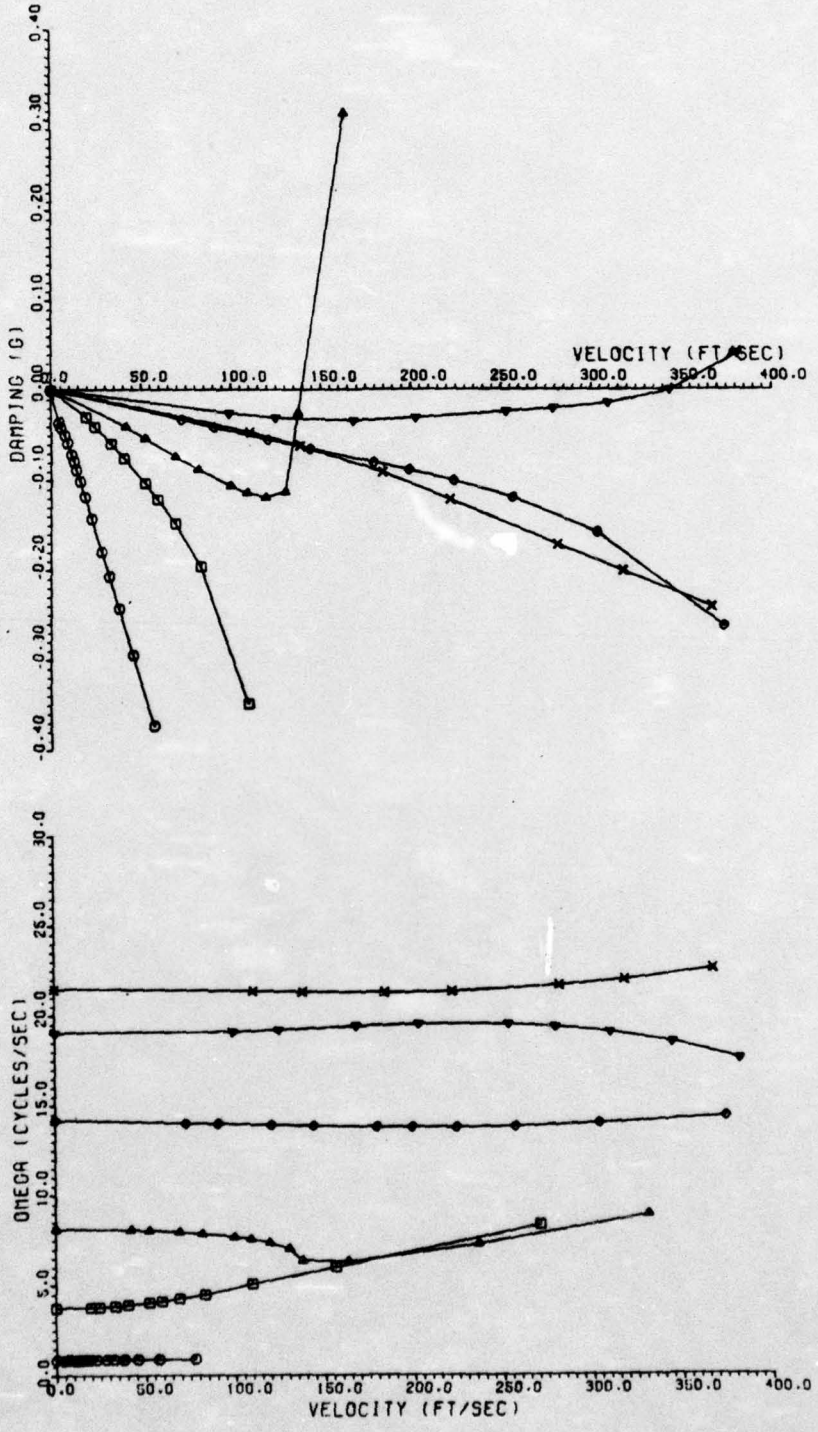

AFFDL 60° , $\frac{\omega_h}{\omega_\theta} = 0.8$, $\bar{X} = 0.9$ FT

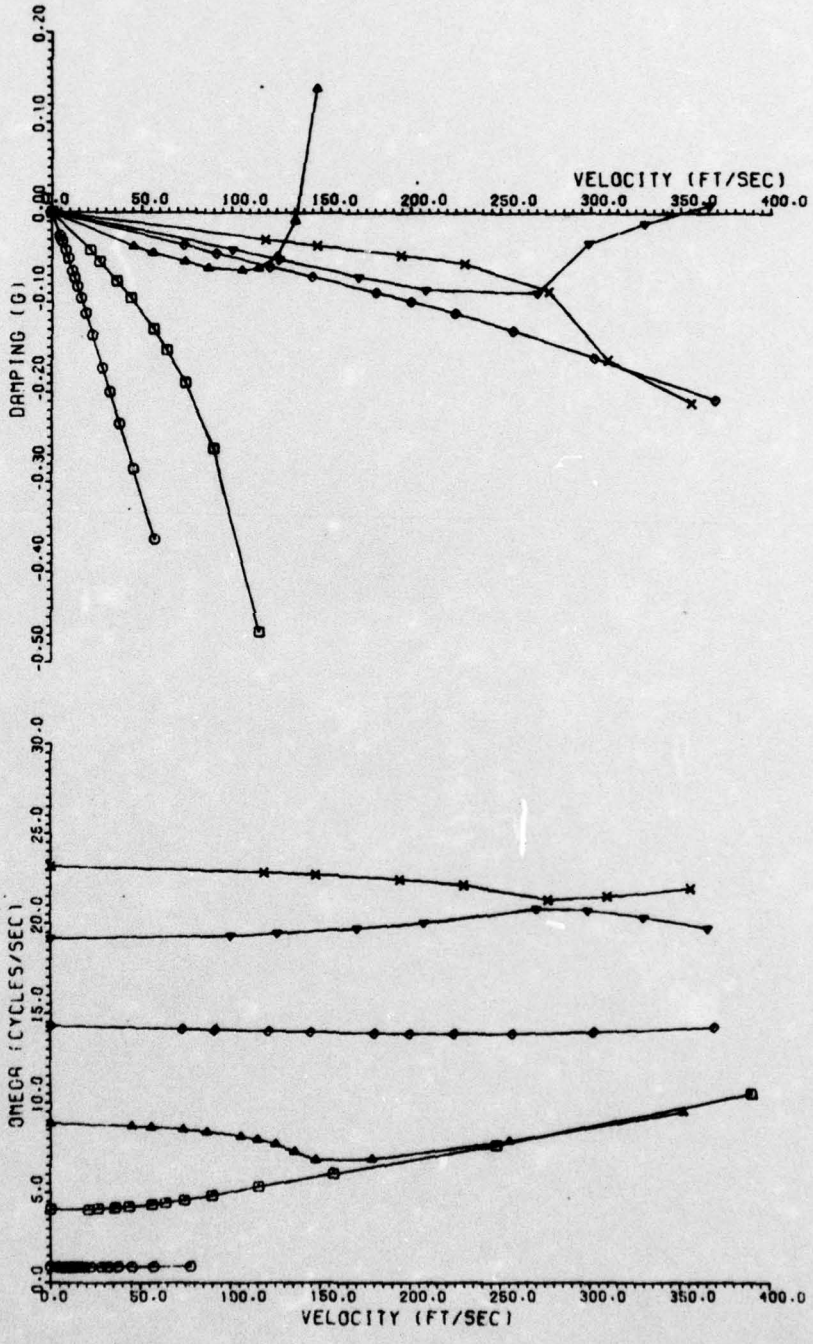

AFFDL 60° , $\frac{\omega_h}{\omega_\theta} = 0.6$, $\bar{X} = 0.25$ FT

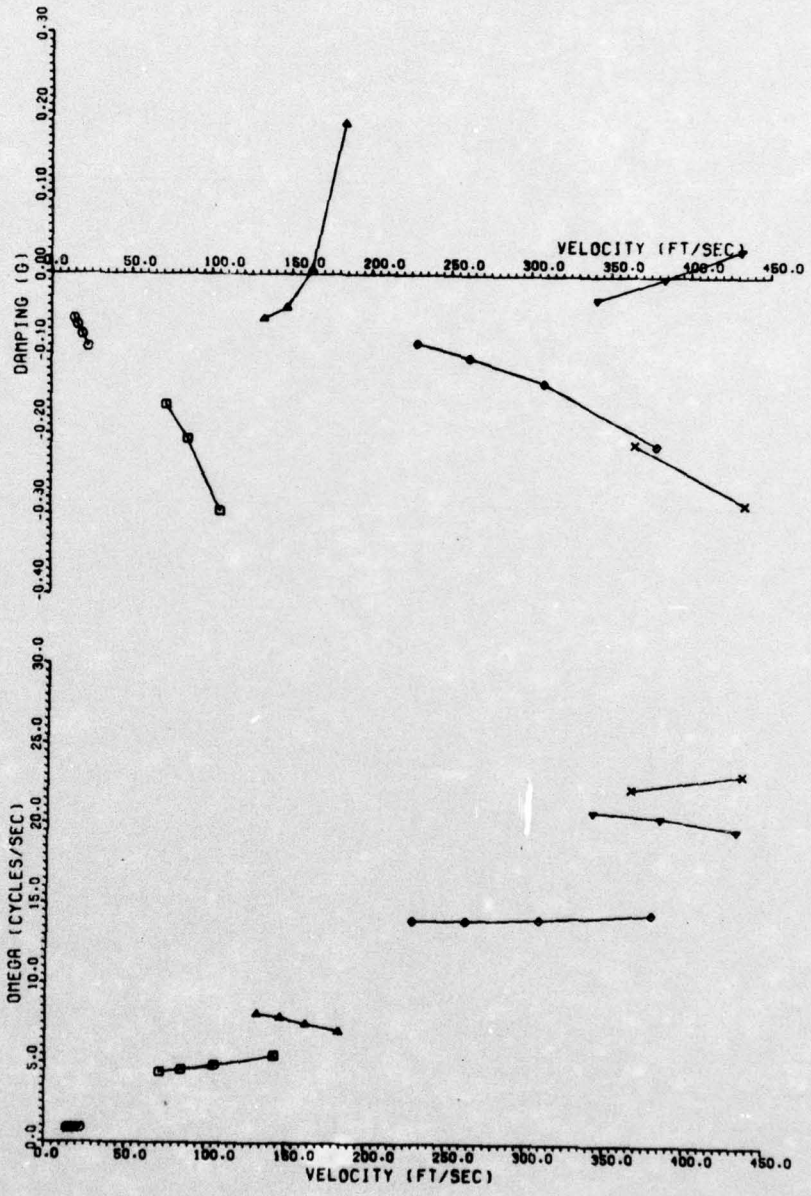

AFFDL 60° , $\frac{\omega_h}{\omega_\theta} = 0.6$, $\bar{X} = .25$ FT , Antisymmetric Aerodynamics

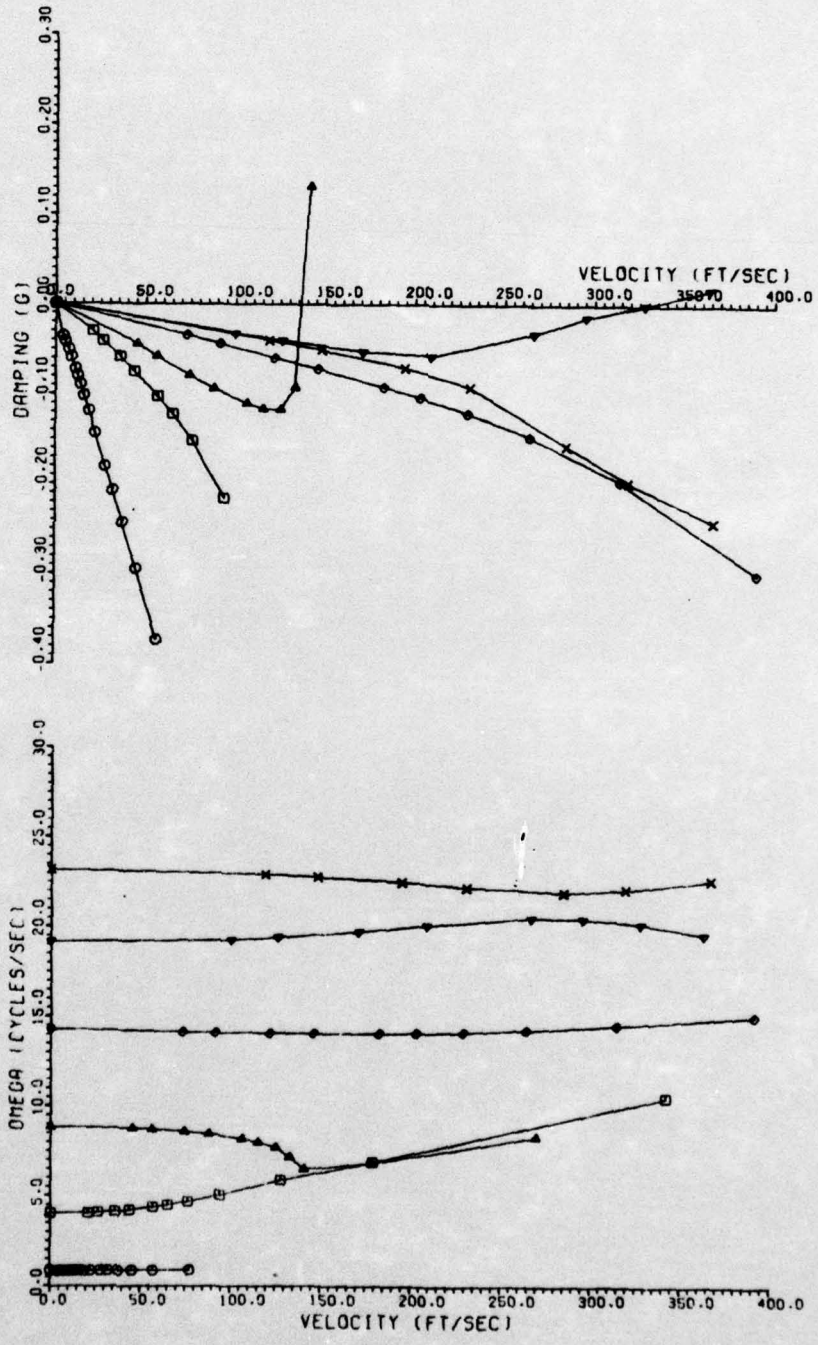

AFFDL 60° , $\frac{\omega_h}{\omega_\theta} = 0.6$, $\bar{X} = 0.9$ FT

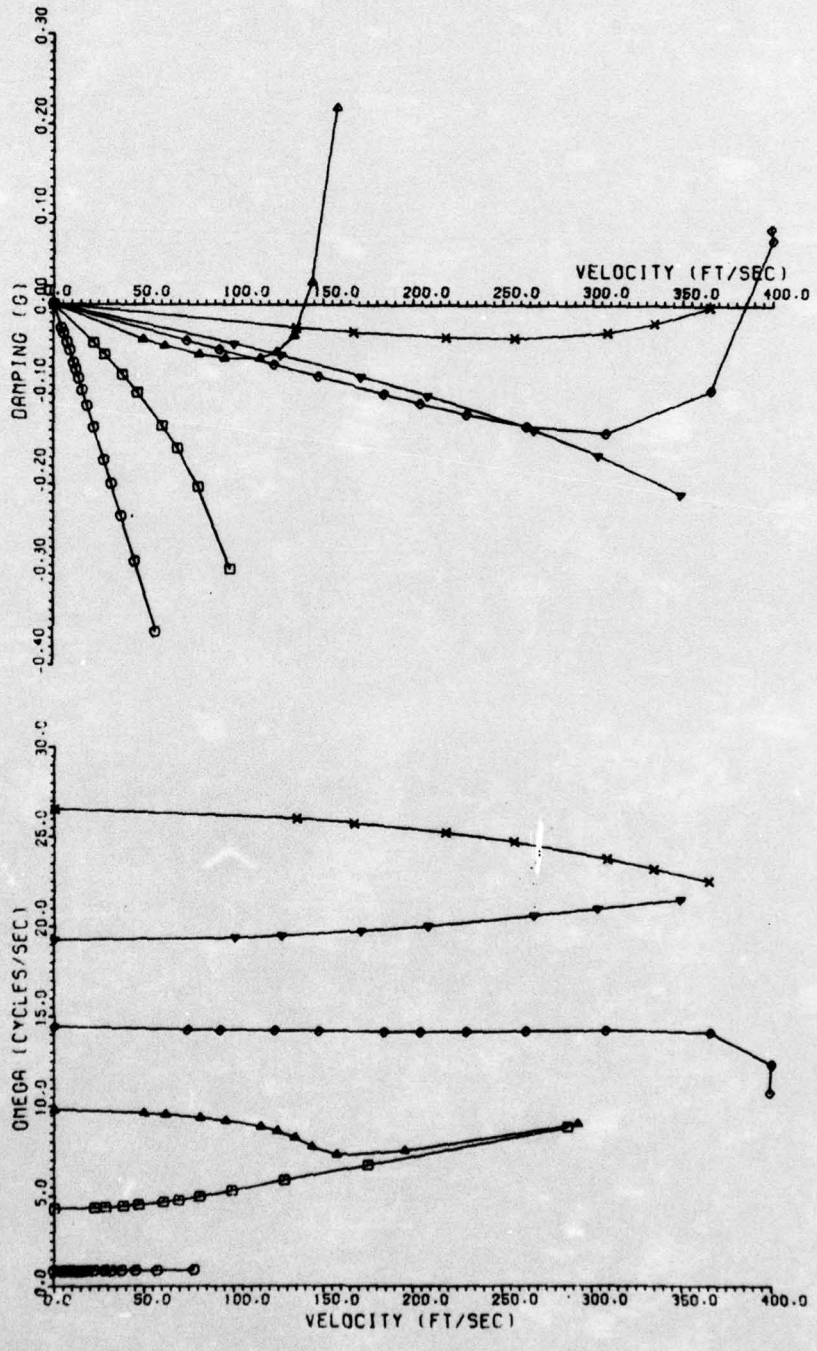

AFFDL 60° , $\frac{\omega_h}{\omega_\theta} = 0.4$, $\bar{X} = 0.25$ FT

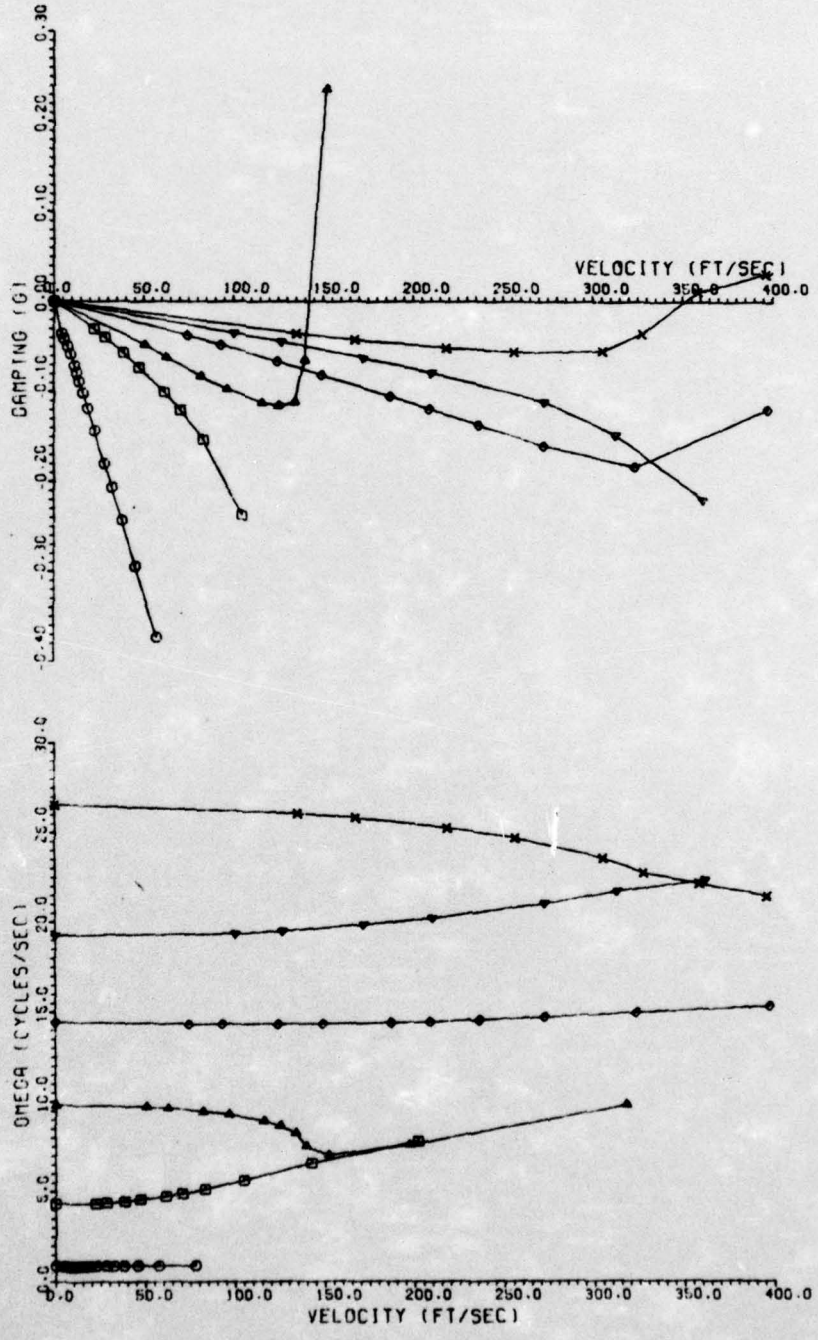

AFFDL 60° , $\frac{\omega_h}{\omega_\theta}$ = 0.4 , $\bar{X}$ = 0.9 FT

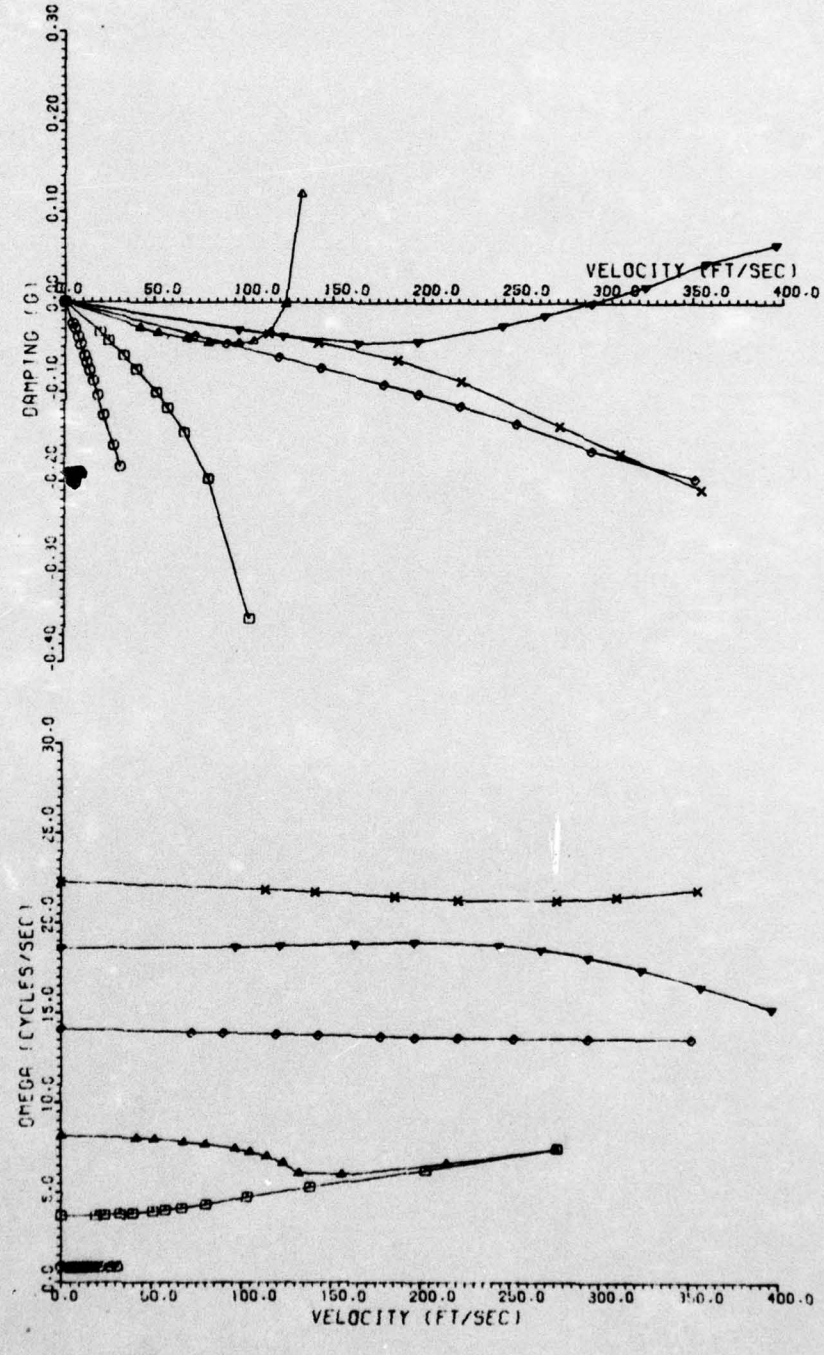

AFFDL 60° , * , $\bar{X}$ = 0.25 FT, M1

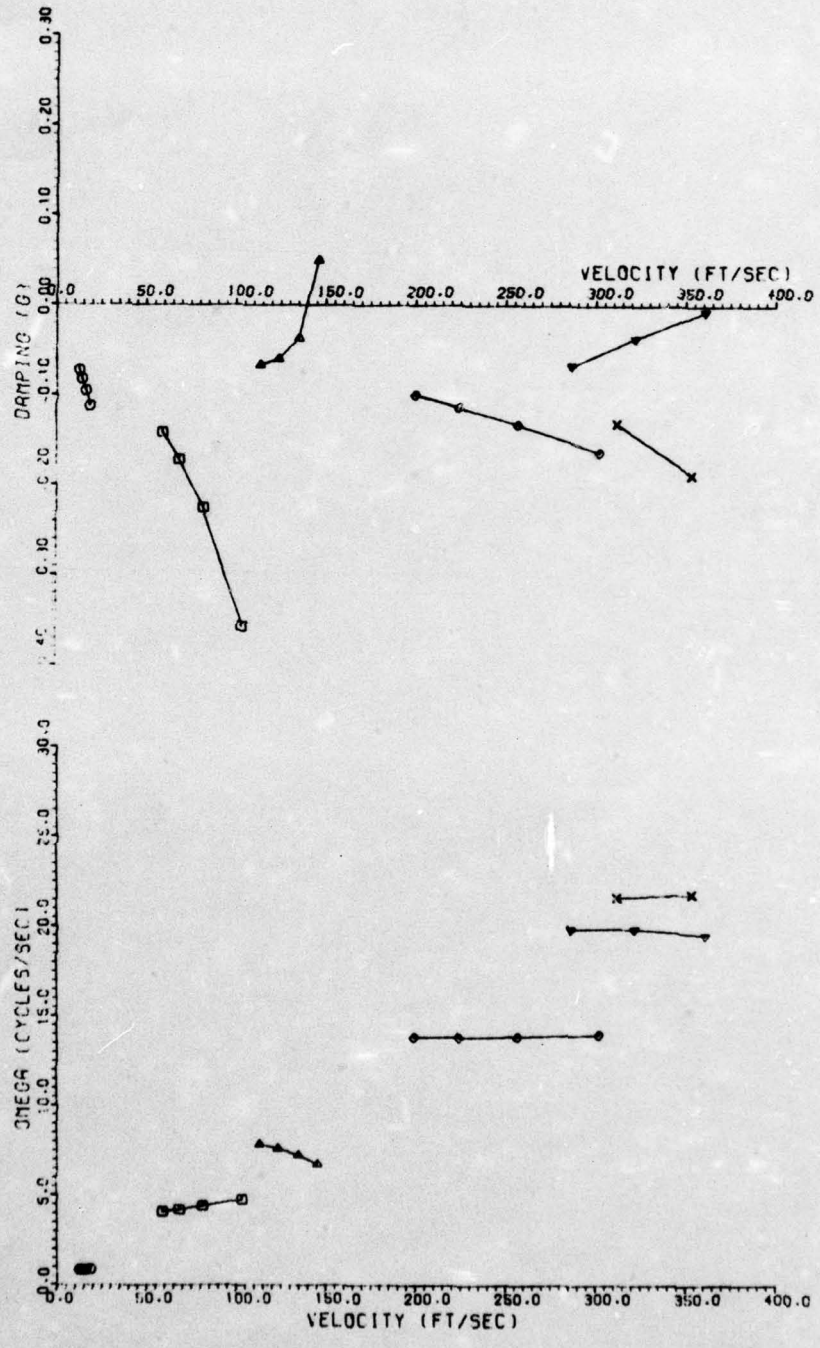

AFFDL 60° , * , $\bar{X}$ = 0.25 FT , R

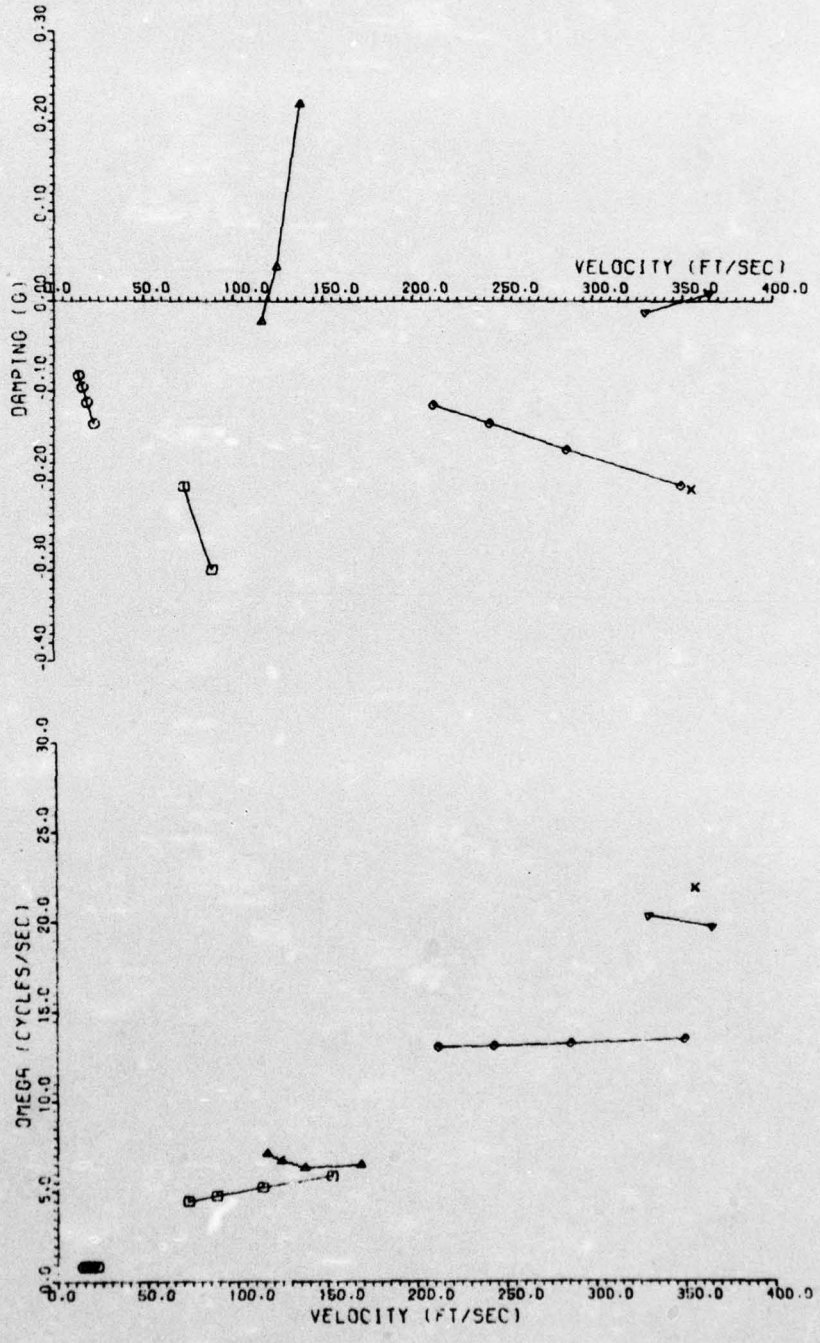

AFFDL 60° , * , $\bar{X}$ = 0.25 FT , P

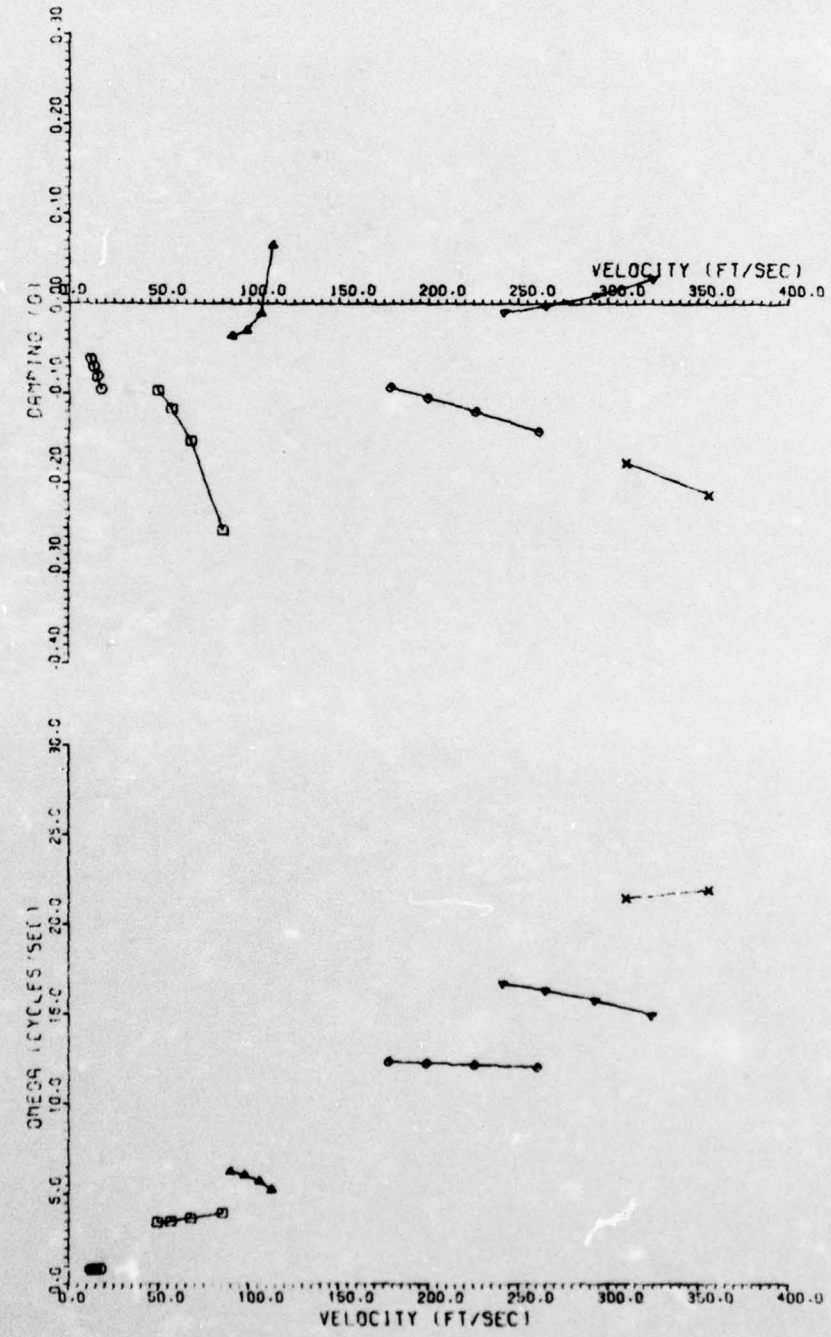

AFFDL 60° , $\frac{\omega_h}{\omega_\theta} = 0.6$, $\bar{X} = 0.25$ FT , PM

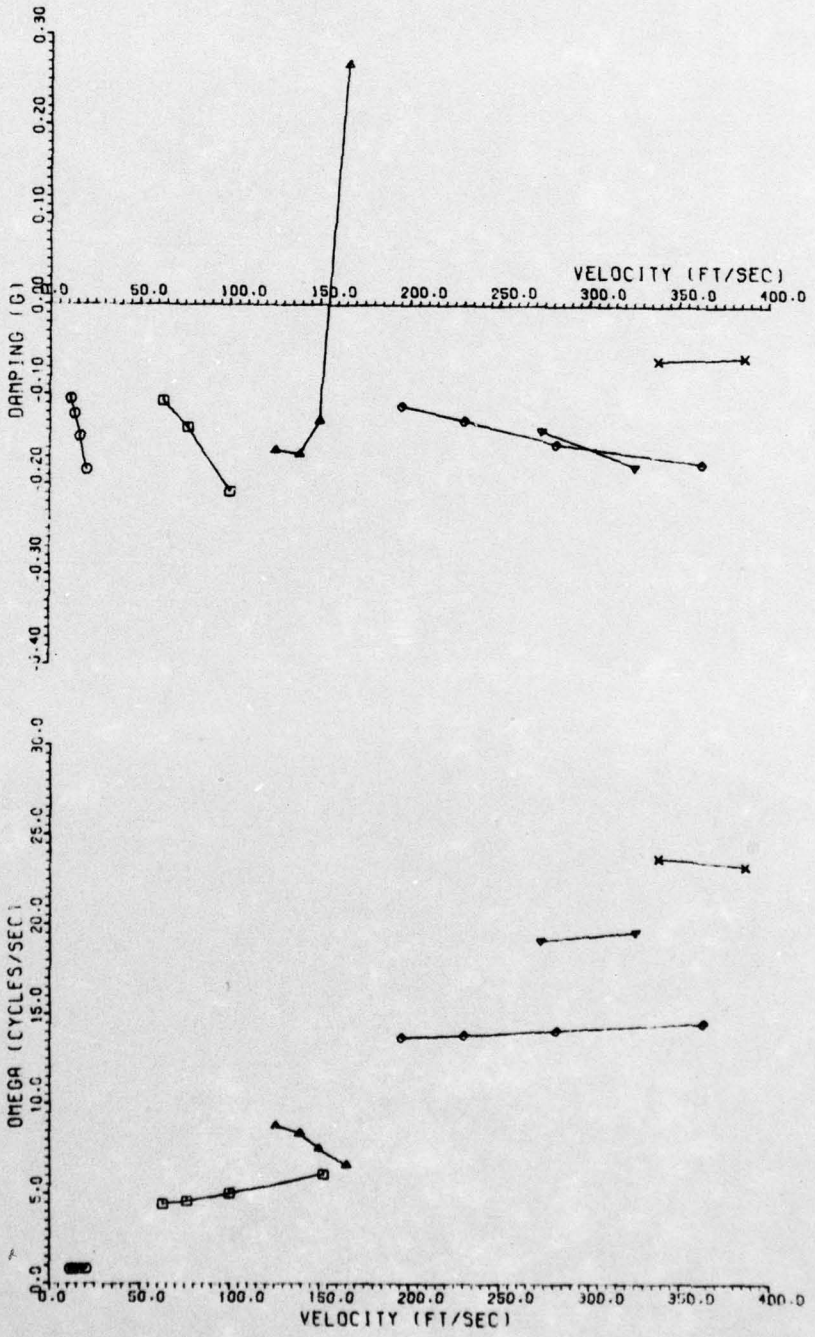

AFFDL 45° , * , $\bar{X}$ = 0.99 FT

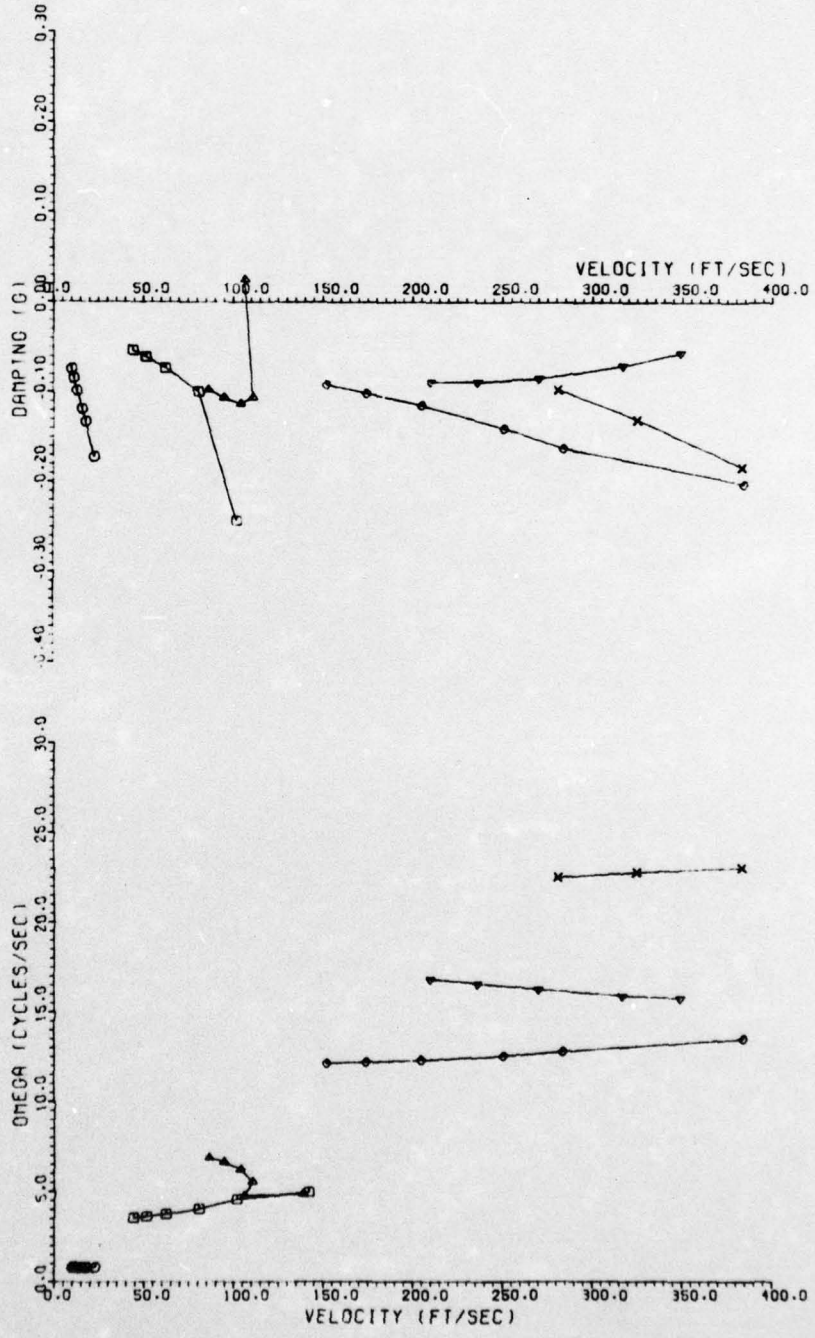

AFFDL 45° , # , $\bar{X}$ = 0.99 FT , PM

AD-A039 245 TEXAS UNIV AT AUSTIN DEPT OF AEROSPACE ENGINEERING AN--ETC F/G 20/4
ANALYTICAL FLUTTER STUDIES OF A SUBSONIC, ACTIVELY CONTROLLED, --ETC(U)
MAR 77 L LEHMAN, R STEARMAN F44620-76-C-0072

UNCLASSIFIED AFOSR-TR-77-0637 NL

2 OF 2
AD A039245

END
DATE FILMED
6-77

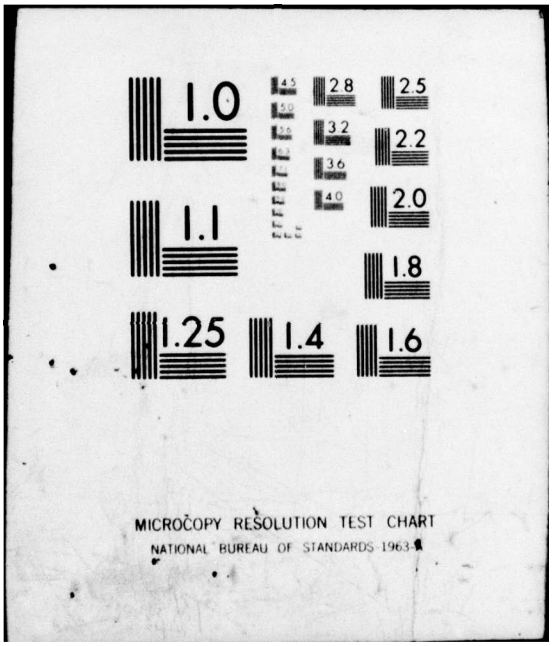
1.0
1.1
1.25
1.4
1.6
1.8
2.0
2.2
2.5
2.8
3.2
3.6
4.0
MICROCOPY RESOLUTION TEST CHART
NATIONAL BUREAU OF STANDARDS 1963-A

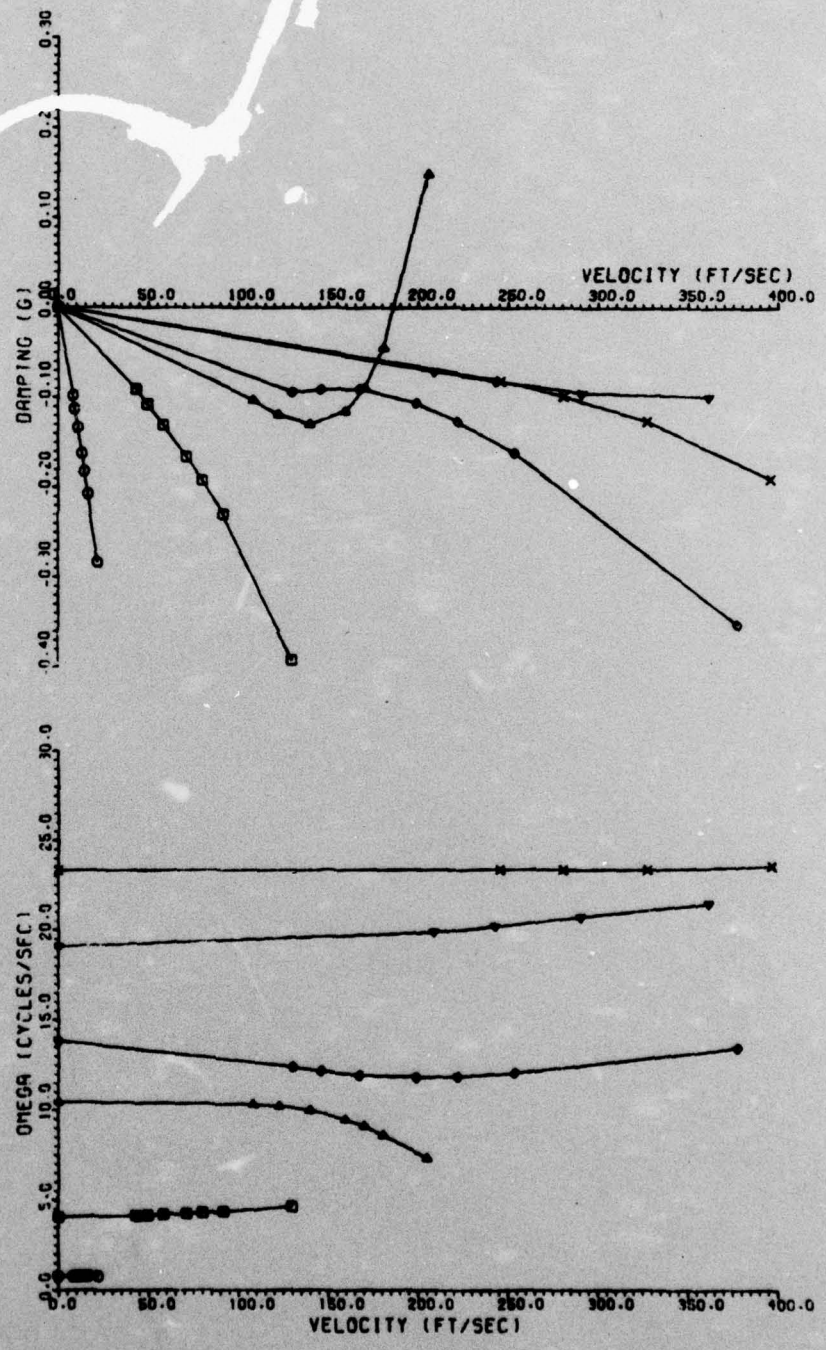

AFFDL 25° , * , $\bar{X}$ = 1.65 FT

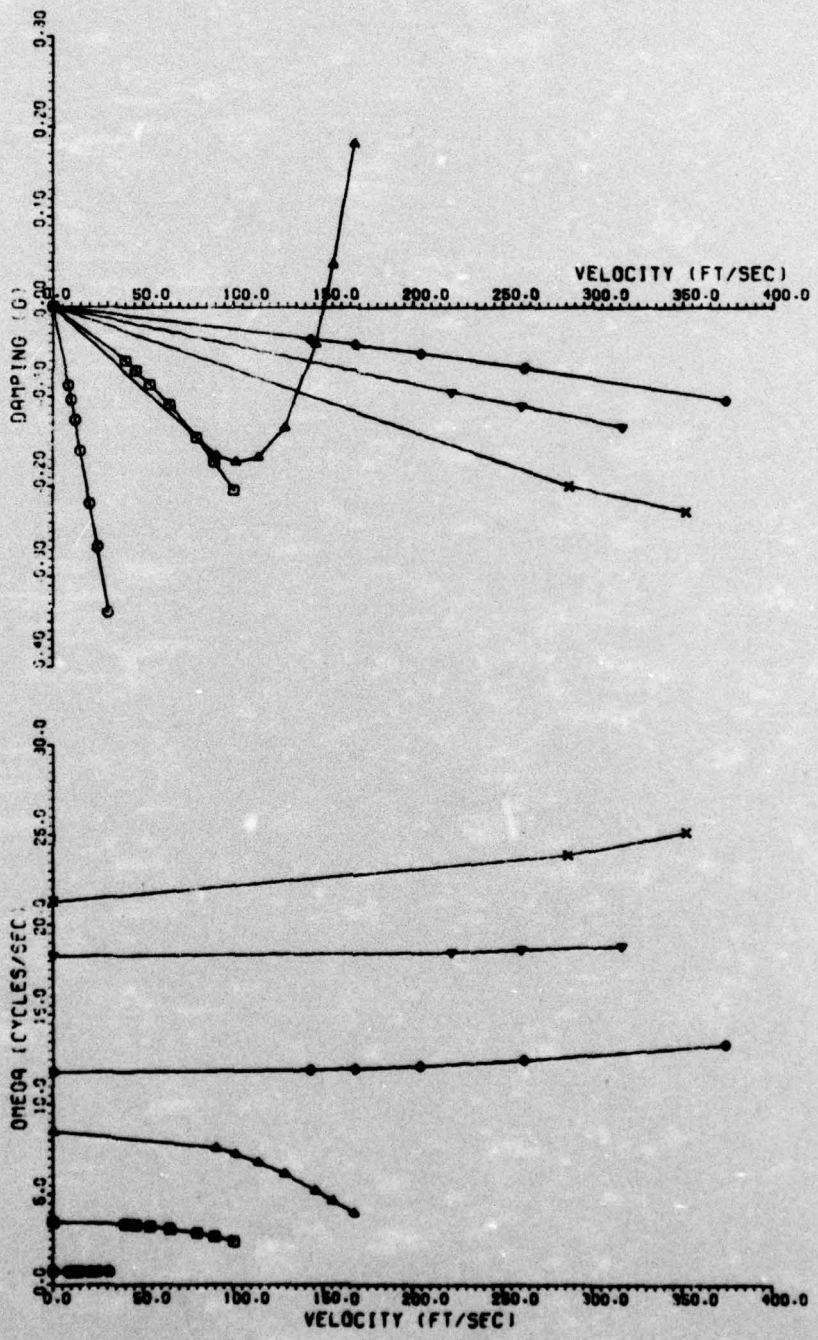

AFFDL 25° , # , $\bar{X}$ = 1.65 FT , PM

APPENDIX E

FLUTTER MODES†

† For abbreviations and symbols, reference Table XV.

FLUTTER MODES

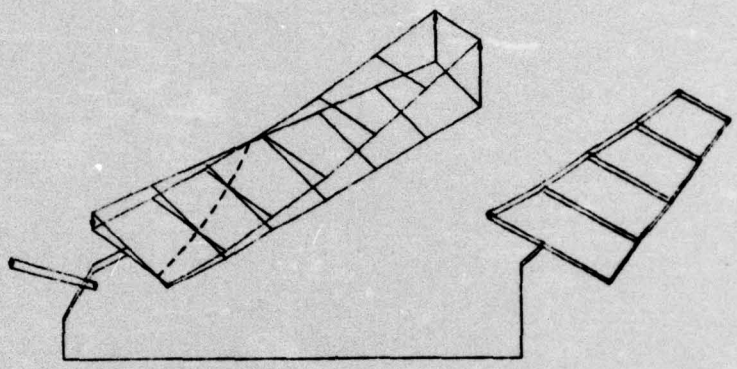

AFFDL 60° , $\frac{\omega_h}{\omega_\theta} = 0.6$, $\bar{X} = 0.25$ FT

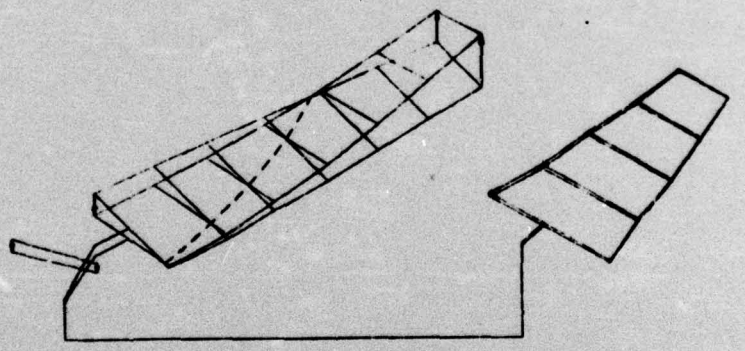

AFFDL 60° , $\frac{\omega_h}{\omega_\theta} = 0.6$, $\bar{X} = 0.25$ FT , PM

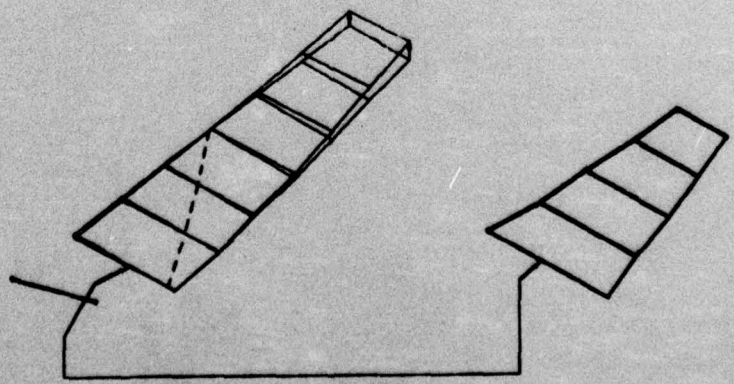

AFFDL 45° , * , $\bar{X} = 0.99$ FT

FLUTTER MODES

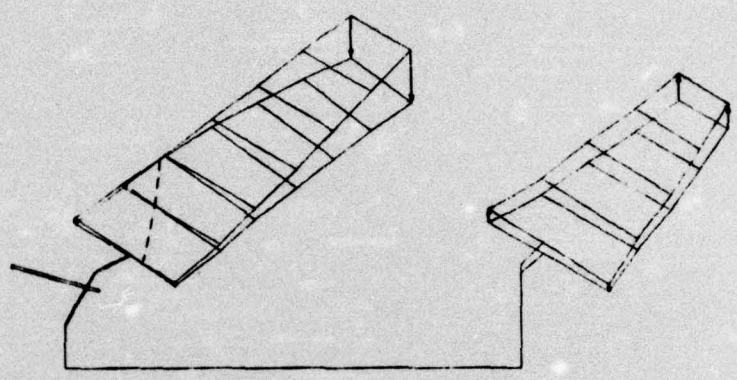

AFFDL 45° , # , $\bar{X}$ = 0.99 FT , PM

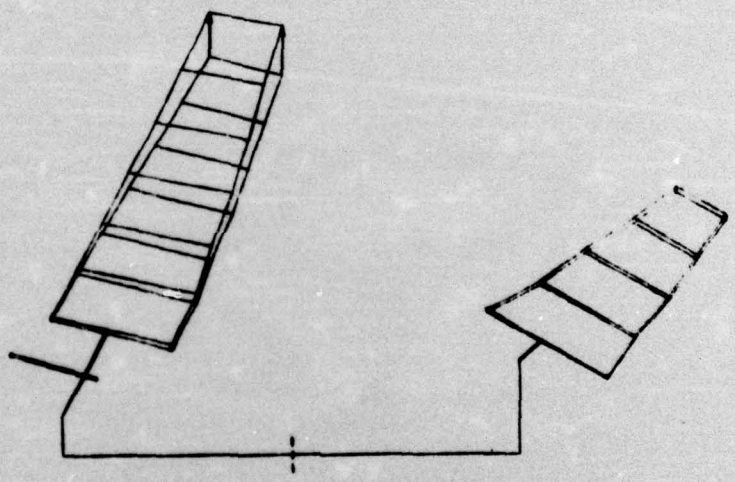

AFFDL 25° , * , $\bar{X}$ = 1.65 FT

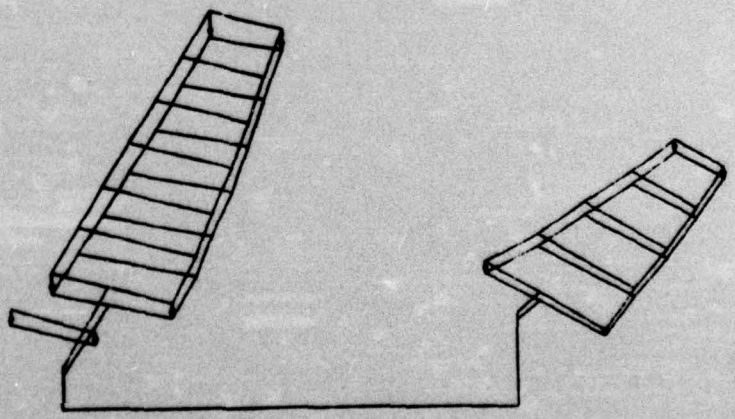

AFFDL 25° , # , $\bar{X}$ = 1.65 FT , PM

BIBLIOGRAPHY

1. Cwach, E.E. and R.O. Stearman, "Suppression of Flutter on Interfering Lifting Surfaces by the Use of Active Controls," AFOSR Interim Report, January 1974.

2. Nissim, E., "Flutter Suppression Using Active Controls Based on the Concept of Aerodynamic Energy," NASA TN D-6199, March 1970.

3. Triplett, W.E., "A Feasibility Study of Active Wing/Store Flutter," Paper 7-B4, AIAA Joint Automatic Control Conference, St. Louis, Mo., August 11-13, 1971.

4. Topp, L.J., "Potential Performance Gains by Use of a Flutter Suppression System," Paper 7-B3, AIAA Joint Automatic Control Conference, St. Louis, Mo., August 11-13, 1971.

5. Sandford, M.C., Abel, I., and D.L. Gray, "A Transonic Study of Active Flutter Suppression Based on an Aerodynamic Energy Concept," AIAA/ASME/SAE 15th Structures, Structural Dynamics, and Materials Conference, Las Vegas, Nevada, April 17-19, 1974.

6. Bolding, R.M. and R.O. Stearman, "The Design, Analysis, and Testing of a Low Budget Wind Tunnel Flutter Model with Active Aerodynamic Controls," AFOSR Scientific Report, January 1976.

7. Griffin, K.E., "Flutter Characteristics and Feedback Suppression Results for Two Modes of Interference Lifting Surface Flutter," Master's Thesis, The University of Texas at Austin, May 1972.

8. Pinnamaneni, R. and R.O. Stearman, "Design and Analysis of Flutter Suppression Systems through the Use of Active Controls," AFOSR Scientific Report, January 1975.

9. Mykytow, W.J., et al., "Subsonic Flutter Characteristics of a Variable Sweep Wing and Horizontal Tail Combination," AFFDL-TR-69-59, November 1970.

10. Martin, D.J. and T. Lauten, "Measurement of Strucutral Influence Coefficients," Manual on Aeroelasticity, Vol. 1, NATO Advisory Group for Aeronautical Research and Development, October 1961.

11. Tong, K.N., Theory of Mechanical Vibration, John Wiley and Sons, Inc., New York, NY, 1960.

12. Fung, Y.C., An Introduction to the Theory of Aeroelasticity, Dover Publications, Inc., New York, NY, 1969.

13. Warburton, G.B., The Dynamical Behavior of Structures, The Macmillan Company, New York, NY, 1964.

14. Bisplinghoff, R.L. and H. Ashley, Principles of Aeroelasticity, Dover Publications, Inc., New York, NY, 1975.

15. Myklestad, N.O., Vibration Analysis, McGraw-Hill Book Company, New York, NY, 1944.

16. Dugundji, J. "On the Calculations of Natural Modes of Free-Free Structures," Journal of the Aerospace Sciences, February 1961.

17. Meirovitch, L., Analytical Methods in Vibrations, The Macmillan Company, New York, NY, 1967.

18. Grumman Aerospace Corporation, "An Automated Procedure for Flutter and Strength Analysis and Optimization of Aerospace Vehicles," AFFDL-TR-75-137, Vol. I: Theory and Application, December 1975.

19. Donato, V.W. and C.R. Huhn, Jr., "Supersonic Unsteady Aerodynamics for Wings with Trailing Edge Control Surfaces and Folded Tips," AFFDL-TR-68-30, August 1968.

20. Albano, E., Perkinson, R., and W.P. Rodden, "Subsonic Lifting-Surface Theory Aerodynamics and Flutter Analysis of Interfering Wing/Horizontal-Tail Configurations," AFFDL-TR-70-59, September 1970.

21. Frederick, W.A., Jr., "A Composite Flutter Analysis Fortran Computer Program for Subsonic and Supersonic Flow," Master's Thesis, The University of Texas at Austin, August 1970.

UNCLASSIFIED

(9) Final rept. 17 Feb 76 - 31 Jan 77

SECURITY CLASSIFICATION OF THIS PAGE (When Data Entered)

REPORT DOCUMENTATION PAGE

READ INSTRUCTIONS BEFORE COMPLETING FORM

1. REPORT NUMBER: (18) AFOSR - TR - 77 - 0637 (19)
2. GOVT ACCESSION NO.
3. RECIPIENT'S CATALOG NUMBER

4. TITLE (and Subtitle): (6) ANALYTICAL FLUTTER STUDIES OF A SUBSONIC, ACTIVELY CONTROLLED, VARIABLE GEOMETRY WIND TUNNEL MODEL, Volume I
5. TYPE OF REPORT & PERIOD COVERED: FINAL 2/1/76 - 1/31/77
6. PERFORMING ORG. REPORT NUMBER

7. AUTHOR(s): (10) Larry Lehman, Ronald Stearman
8. CONTRACT OR GRANT NUMBER(s): (15) F44620-76-C-0072

9. PERFORMING ORGANIZATION NAME AND ADDRESS: The University of Texas at Austin, Dept. of Aerospace Engr. and Engr. Mechanics, Austin, Texas 78712
10. PROGRAM ELEMENT, PROJECT, TASK AREA & WORK UNIT NUMBERS: ~~9782-04~~ 2307/B1

11. CONTROLLING OFFICE NAME AND ADDRESS: Air Force Office of Scientific Research/NA, Building 410, Bolling Air Force Base, D.C. 20332
12. REPORT DATE: (11) Mar[illegible]77
13. NUMBER OF PAGES: 101 (125 103 p.)

14. MONITORING AGENCY NAME & ADDRESS (if different from Controlling Office): (16) 2307 (12) B1
15. SECURITY CLASS. (of this report): UNCLASSIFIED
15a. DECLASSIFICATION/DOWNGRADING SCHEDULE

16. DISTRIBUTION STATEMENT (of this Report)

APPROVED FOR PUBLIC RELEASE; DISTRIBUTION UNLIMITED.

17. DISTRIBUTION STATEMENT (of the abstract entered in Block 20, if different from Report)

18. SUPPLEMENTARY NOTES

19. KEY WORDS (Continue on reverse side if necessary and identify by block number)

Flutter Suppression
Active Control
Wind Tunnel Flutter Model

20. ABSTRACT (Continue on reverse side if necessary and identify by block number)

A structural dynamic system identification was experimentally conducted on a wind tunnel flutter model with active aerodynamic controls. Mass and stiffness parameters were varied on the model to determine an optimum configuration for the wind tunnel tests.

402465

DD FORM 1 JAN 73 1473 EDITION OF 1 NOV 65 IS OBSOLETE

UNCLASSIFIED

SECURITY CLASSIFICATION OF THIS PAGE (When Data Entered)